

Meta-topological hydrogel enables multisource and frequency-tailored artefact mitigation for bioelectronics

Received: 25 September 2025

Accepted: 25 February 2026

Published online: 24 March 2026

 Check for updates

Guo Tian¹, Longchao Huang², Xinglong Pan¹, Zhiwei Li¹, Wanheng Lu¹, Wei Li Ong¹, Chang Liu¹, Yi Zhou¹, Yue Sun², Weili Deng², Weiqing Yang², Wei Gao³ & Ghim Wei Ho^{1,4}

High-fidelity signal acquisition underpins next-generation healthcare bioelectronics, yet motion artefacts severely impair both signal integrity and measurement reliability. Existing mitigation strategies primarily target a single artefact type or a fixed frequency range, limiting scalability and generality. Here we report a meta-topological hydrogel that combines programmable phononic metastructure filtering with topology-tunable ion diffusion to suppress multisource mechanical and biopotential artefacts across tailored frequency ranges. This artefact-mitigating platform enables simultaneous, artefact-free acquisition of haemodynamic and electrophysiological signals, achieving ISO-grade A blood pressure accuracy and an electrocardiograph signal-to-noise ratio of 37.36 dB during daily activities. The platform supports robust feature extraction from physiological signals for fatigue profiling, achieving a deep learning classification accuracy of 92.04%. We further demonstrate effective artefact suppression across diverse biosignals modalities, including heart and respiratory sounds, voice, electroencephalogram and electrooculogram, highlighting its potential for scalable and kinematic-tolerant monitoring in motion-intensive scenarios.

Wearable bioelectronics hold great promise for continuous health monitoring in real-life settings^{1–6}. Dynamic environments introduce complex motion artefacts from muscle activity, body movement and physiological interference, severely degrading signal quality and limiting practical deployment^{7–9} (Supplementary Fig. 1). While materials engineering^{10,11}, device design^{12,13} and algorithmic correction^{4,14} are mainstream strategies for mitigating motion artefacts, most methods target only a single artefact type or fixed frequency band, failing to address real-world complexities^{15–18}. This challenge is especially

evident in mental-health-related conditions, such as chronic fatigue, a multifactorial condition involving cognitive overload, circadian disruption and physical exertion, for which no single physiological marker is diagnostic^{19–21}.

Chronic fatigue affects approximately 13.5% of adults in the USA and contributes to a substantial societal and economic burden, particularly in high-risk professions where fatigue increases the likelihood of human error^{22,23} (Fig. 1a and Supplementary Fig. 2). These realities underscore the pressing need for continuous, real-time fatigue

¹Department of Electrical and Computer Engineering, National University of Singapore, Singapore, Singapore. ²Key Laboratory of Advanced Technologies of Materials (Ministry of Education), School of Materials Science and Engineering, Southwest Jiaotong University, Chengdu, China. ³Andrew and Peggy Cherng Department of Medical Engineering, Division of Engineering and Applied Science, California Institute of Technology, Pasadena, CA, USA.

⁴Department of Materials Science and Engineering, National University of Singapore, Singapore, Singapore. ✉e-mail: wqyang@swjtu.edu.cn; weigao@caltech.edu; elehgw@nus.edu.sg

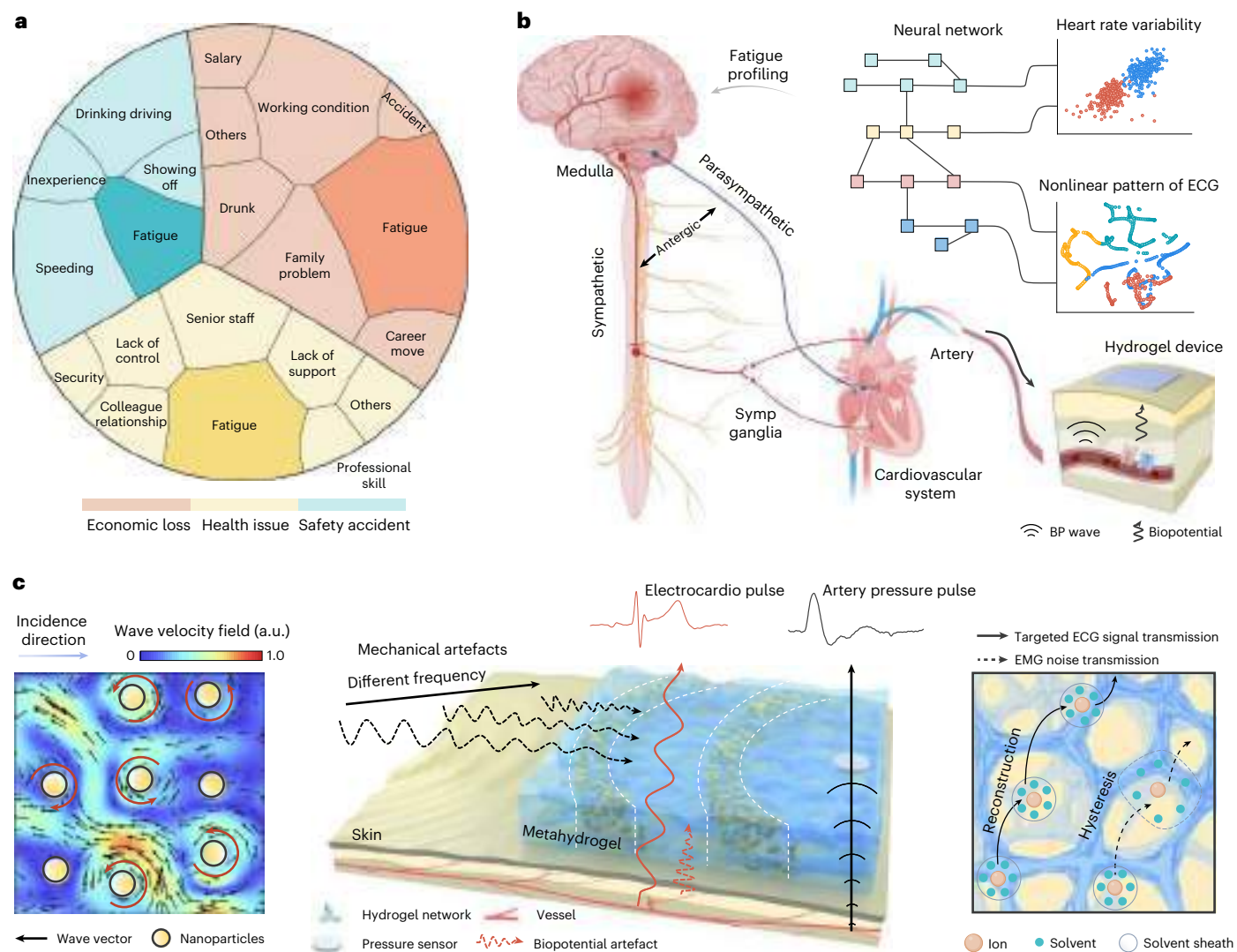


Fig. 1 | Overview of the MAP for fatigue profiling. a, Impact of fatigue including economic loss, health issues and safety accidents, where the area associated with each factor represents its relative magnitude of impact. **b**, Illustration of the metahydrogel platform that collects electrophysiological and haemodynamic information and performs machine learning powered fatigue evaluation. **c**, Working mechanism of metahydrogel for collecting targeted signals and attenuating concomitant artefacts. Left: mechanical interference is blocked and

dissipated by local resonance. Right: biopotential artefacts are filtered through frequency-selective ionic mobility, as solvation reconstruction dynamics do not respond at EMG frequencies. Schematics in **b** created in BioRender: brain, Tian, G. <https://biorender.com/odm98mm> (2026); spinal cord, Tian, G. <https://biorender.com/ckttg2c> (2026); heart, Tian, G. <https://biorender.com/2540e4r> (2026); vessel, Tian, G. <https://biorender.com/hl83bbg> (2026).

assessment systems that operate reliably in daily settings characterized by motion and environmental variability. Among various biomarkers, such as brain activity²⁴, biochemical markers^{25,26} and cardiovascular patterns^{27–30}, wearable cardiovascular monitoring is particularly attractive for fatigue profiling owing to its portability and data processing efficiency. As cardiovascular states are regulated by the autonomic nervous system (Fig. 1b), electrocardiographic and haemodynamic signals serve as robust indicators of fatigue (Supplementary Note 1), provided motion artefacts are effectively mitigated.

To address this challenge, we developed a meta-topological hydrogel that seamlessly integrates mechanical wave-modulating metastructures with topological-tuned ionic transport, facilitating programmable and targeted suppression of dynamically evolving motion artefacts. The coined metahydrogel artefact-mitigating platform (MAP) functions as an integrated noise cancellation interface for high-fidelity haemodynamic and electrophysiological signals acquisition for fatigue profiling and broader bioelectronics applications (Fig. 1c).

Periodically assembled nanoparticles patterns within the hydrogel scatter mechanical waves to mitigate mechanical artefacts (Fig. 1c, left), while frequencies-selective ion migration, modulated through solvation structure design, mitigates biopotential interference (Fig. 1c, right). Structural and electrolyte optimization aligns the filtering behaviour with physiological noise spectra, and an autoencoder-based denoising algorithm suppresses transient, unstructured noise with preserving critical physiological features. Under dynamic conditions, this synergistic platform achieves an ECG signal-to-noise ratio (SNR) of 37.36 dB, while reducing systolic/diastolic blood pressure (SBP/DBP) measurement errors from $3.45 \pm 10.99/2.02 \pm 8.99$ mm Hg to $0.37 \pm 4.53/0.27 \pm 3.71$ mm Hg. By integrating extracted signal features with cardiovascular patterns, we developed a convolutional neural network and regression model to profile physiological patterns and classify fatigue levels, achieving an accuracy of 92.04% in daily fatigue monitoring. Beyond fatigue tracking, MAP generalizes to diverse biosignals, including heart sounds, respiratory sounds,

voice, electroencephalography and electrooculogram. Hence, MAP establishes a scalable framework for high-fidelity, artefact-free bioelectronics suitable for deployment in real-world settings.

Mechanical damping effect of metastructured hydrogel

Unlike conventional damping materials that lack frequency selectivity and attenuate mechanical signals indiscriminately, a periodic precipitation pattern (Liesegang pattern) was introduced into a polyacrylamide (PAAm) hydrogel to construct a metastructured interface material capable of selectively decoupling mechanical waves (Supplementary Video 1). This self-assembled, ordered pattern was prepared through coupled reactant transport and precipitation kinetics (Fig. 2a and Supplementary Fig. 3). Cross-sectional imaging reveals a periodic $\text{CuCl}_2/\text{K}_2\text{CrO}_4$ precipitation pattern (Fig. 2b), composed of CuCrO_4 nanoparticles separated by depleted regions (Supplementary Figs. 4 and 5). The prenucleation mechanism was confirmed by experimental structural analysis and growth simulation (Supplementary Figs. 6 and 7 and Supplementary Note 2). Based on this mechanism, a stamping method was developed for large-scale fabrication of independent, periodic precipitation structures, highlighting its scalability (Fig. 2c and Supplementary Fig. 8).

Mechanical wave propagation tests confirmed that the periodic precipitation bands interrupted wave propagation (Extended Data Fig. 1). Simulations of the wave propagation and flow-field distribution further validated that the bulk of mechanical energy was absorbed by these nanoparticle structures³¹ (Fig. 2d and Supplementary Figs. 9 and 10). When arranged periodically, these resonators form a continuous frequency band, creating a frequency-selective phononic bandgap that blocks mechanical wave within defined ranges³². Denoising performance was assessed by comparing the fidelity of output signals under noise interference conditions, where the metahydrogel improved signal fidelity from 0.14 to 0.72 (Supplementary Fig. 11). Dynamic rheological measurements of metahydrogel exhibit a high loss factor of 4.18 at 0.1 Hz, indicating efficient mechanical energy dissipation (Supplementary Fig. 12). To benchmark performance, we compared the metahydrogel with conventional damping materials using an Ashby plot (Fig. 2e and Supplementary Table 1). To quantify the allowable dissipated energy, we introduced the loss-to-modulus product (ηE). With a loss factor of 4.18 and a modulus of 0.8 MPa ($\eta E = 3.34$ MPa), the metahydrogel outperforms most conventional materials and hydrogels. Unlike traditional damping hydrogels constrained by an inherent trade-off between compliance and energy dissipation, the local resonance mechanism decouples softness from damping, surpassing the Ashby limit for soft matter³³. Moreover, its modulus closely matches that of biological tissue, enabling conformal interface contact for accurate physiological signal monitoring³⁴.

Mechanical artefact-free haemodynamic monitoring

Compared with conventional hydrogel damping materials that dissipate energy through non-selective structural deformation or bond reconfiguration, the metahydrogel forms a phononic bandgap via its periodic precipitation architecture, enabling frequency-selective damping. To validate tunability, metahydrogels with varying structural parameters were synthesized by modulating ion diffusion and the resulting precipitation patterns (Supplementary Fig. 13). Vibration transmission measurements and transfer-function analyses confirm structure-dependent characteristic damping frequencies, (Fig. 2f and Supplementary Fig. 14), enabling the metahydrogel to be tailored for specific application scenarios. We further systematically explored the effects of precursor thickness, rheology and gelation rate on pattern formation and the resulting damping performance (Extended Data Figs. 2 and 3). The modulus, size and mass of the precipitated particles, as well as the overall dimensions of the patterned region and the number of precipitation bands, were found to exert non-negligible effects on mechanical attenuation performance (Supplementary Fig. 15). Considering both the effective

damping range and the characteristic frequency of motion artefacts, the metahydrogel with a thickness of 2 mm and a structure factor (P) of 1.187 was selected for subsequent applications.

Metahydrogels composed of different materials were synthesized to validate the universality of the damping effect, as distinct diffusion coefficients and reaction kinetics generated varied precipitation patterns (Extended Data Fig. 4a and Supplementary Note 3). Simulations confirmed that these material systems exhibit specific bandgaps across different frequency bands (Extended Data Fig. 4b,c), indicating that damping behaviour can be precisely tuned through material and structural design to cover frequencies relevant to human motion (0.5–30 Hz). Under multidirectional noise interference, the metahydrogel preserved vertical signal integrity by attenuating in-plane wave (Fig. 2g). The coefficient of variation in signal intensity is 0.03 for metahydrogel compared with 0.14 for polydimethylsiloxane (PDMS), highlighting superior noise-mitigation performance. Stable signal acquisition was maintained under impulsive disturbances as well (Supplementary Fig. 16). In addition, a comparison of the SNR of transmitted perpendicular vibration amplitude through metahydrogel and other commercial damping materials confirms its selective sensitivity to low-frequency physiological signals (Supplementary Figs. 17 and 18).

To determine suitability for skin-interfacing bioelectronics, the biocompatibility, permeability and adhesivity of metahydrogels were assessed. Due to the encapsulation of nanoparticles within the hydrogel matrix and negligible ionic leakage, there is no observable cellular damage when cocultured with epithelial cells (Supplementary Fig. 19). The porous network enables a water vapour transmission rate of $2.43 \text{ kg m}^{-2} \text{ day}^{-1}$, exceeding the average human skin permeability ($\sim 0.6 \text{ kg m}^{-2} \text{ day}^{-1}$)³⁵, thus facilitating efficient moisture exchange (Supplementary Fig. 20). Furthermore, incorporation of gelatin enables temperature-triggered reversible adhesion, minimizing the risk of tissue damage (Supplementary Fig. 21). Together with the moisture-retaining properties arising from the electrolyte solution within the hydrogel, it can maintain internal water balance under prolonged use and extreme environmental conditions, thereby ensuring stable mechanical, electrical and sensing performance (Supplementary Figs. 22–24). Mechanical durability tests showed no interfacial fatigue or structural failure under cyclic stretching or high strain (Supplementary Fig. 25), and notched tensile tests confirmed efficient energy dissipation by the metastructure (Supplementary Video 2). We further compared the damping and mechanical performance of the metahydrogel against other commercial polymeric dampers (Supplementary Fig. 26), where it demonstrated superiority across all evaluated metrics. Leveraging this bioelectronic platform, a commercial piezoelectric film sensor was integrated to capture artefact-free haemodynamic data.

Because the arterial pressure signal is weak (<10 kPa) and highly susceptible to mechanical artefacts^{36,37}, we assessed the sensor sensitivity to confirm its suitability for blood pressure (BP) monitoring. The integrated sensor achieves a sensitivity of 63.3 mV kPa^{-1} (Supplementary Fig. 27), and wrist-mounted measurements further show effective artefact suppression compared with direct sensor recording (Supplementary Figs. 28 and 29 and Supplementary Note 4). Bland–Altman analysis reveals that the metahydrogel reduces measurement errors from $2.53 \pm 13.83/2.14 \pm 10.05 \text{ mm Hg}$ to $0.24 \pm 4.35/0.16 \pm 4.64 \text{ mm Hg}$ for SBP/DBP, respectively (Supplementary Fig. 30). Four-quadrant plot analysis further confirmed the improved consistency of the metahydrogel (86.7% for SBP and 90.3% for DBP) relative to direct measurements (55.2% for SBP and 52.2% for DBP; Fig. 2h). These results establish the metahydrogel as a robust foundation for accurate BP monitoring and subsequent physiological assessments.

Biopotential artefact mitigation for ECG monitoring

Biopotential artefacts stem from the electrochemical activities in nervous and muscular cells, with electromyography (EMG) being the

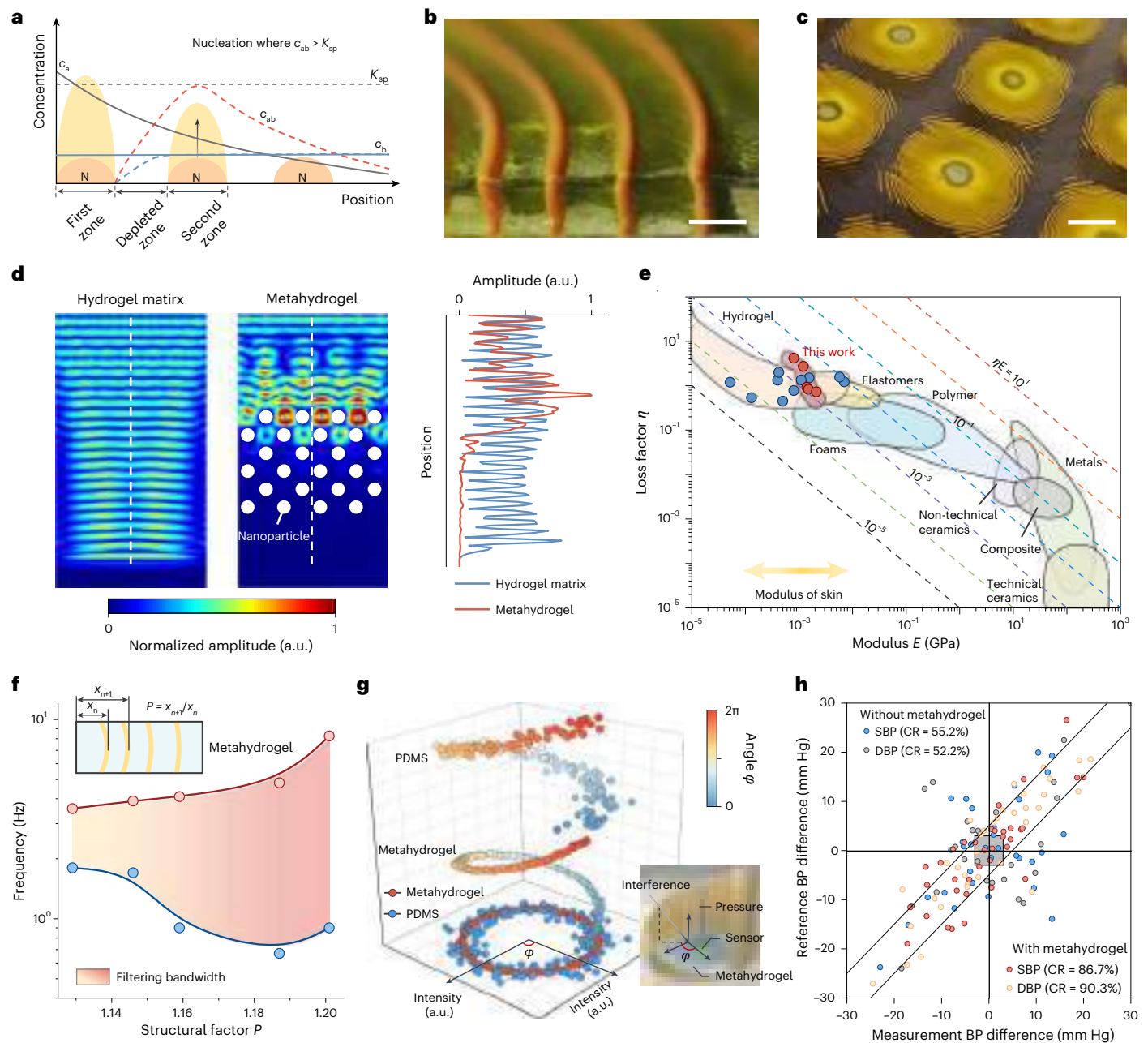


Fig. 2 | Mitigation of mechanical artefact by the metahydrogel platform.

a, Schematic nucleation and periodic pattern growth model based on supersaturation theory. As the ion concentration (c_{ab}) exceeds the critical supersaturation (K_{sp}), nucleation and pattern growth are initiated to form the first precipitation region. Back-diffusion of electrolyte within the matrix creates a depleted zone, followed by iterative reactions and ionic diffusion. **b, c**, Photographs of cross-sectional morphology of $\text{CuCl}_2/\text{K}_2\text{CrO}_4$ periodic pattern (**b**) and the large-scale fabrication via stamp method (**c**). Scale bars, 2 mm (**b**) and 3 cm (**c**). Experiments were independently repeated at least three times ($n = 3$) with consistent results. **d**, Simulated mechanical wave propagation in hydrogel matrix and metahydrogel. Right curves present the amplitude as marked by the dashed white line. **e**, Ashby plot of loss factor (η) and modulus (E)

of metahydrogel and other damping materials. The dashed lines represent the materials with different ηE products. **f**, Damping frequency versus structural factor of metahydrogel. The inset shows the definition of structural factor $P = x_{n+1}/x_n$, where x_n denotes the distance of the n th band measured from the reaction centre. **g**, Evaluation of resistance to three-dimensional force interference. The inset schematically shows the test set-up, and the projection on the bottom plane indicates the signal intensity detected by the sensor. **h**, Four-quadrant plot and CRs for evaluating BP measurement accuracy using a commercial sphygmomanometer and a piezoelectric sensor with or without the metahydrogel. Diagonal black lines indicate the ± 5 mm Hg error bars, and the grey area represents the ± 3 mm Hg exclusion zone.

dominant interference source in ECG monitoring³⁸. Because EMG amplitudes are comparable to or even exceed ECG signals, spectral overlap between ECG (0.1–100 Hz) and EMG (20–500 Hz) can severely distort recordings. Frequency energy analysis (Extended Data Fig. 5) shows that ECG energy is concentrated primarily within 0.1–30 Hz (>97%), while more than 90% of the EMG energy lies above 30 Hz,

supporting the feasibility of selectively attenuating EMG without compromising ECG signals (Fig. 3a). This spectral separation enables frequency-selective biopotential filtering via ionic transport engineering. Based on the vehicular transport mechanism of ions in the electrolyte solution (Supplementary Fig. 31), the ion migration is strongly associated with the bonding interactions between ions

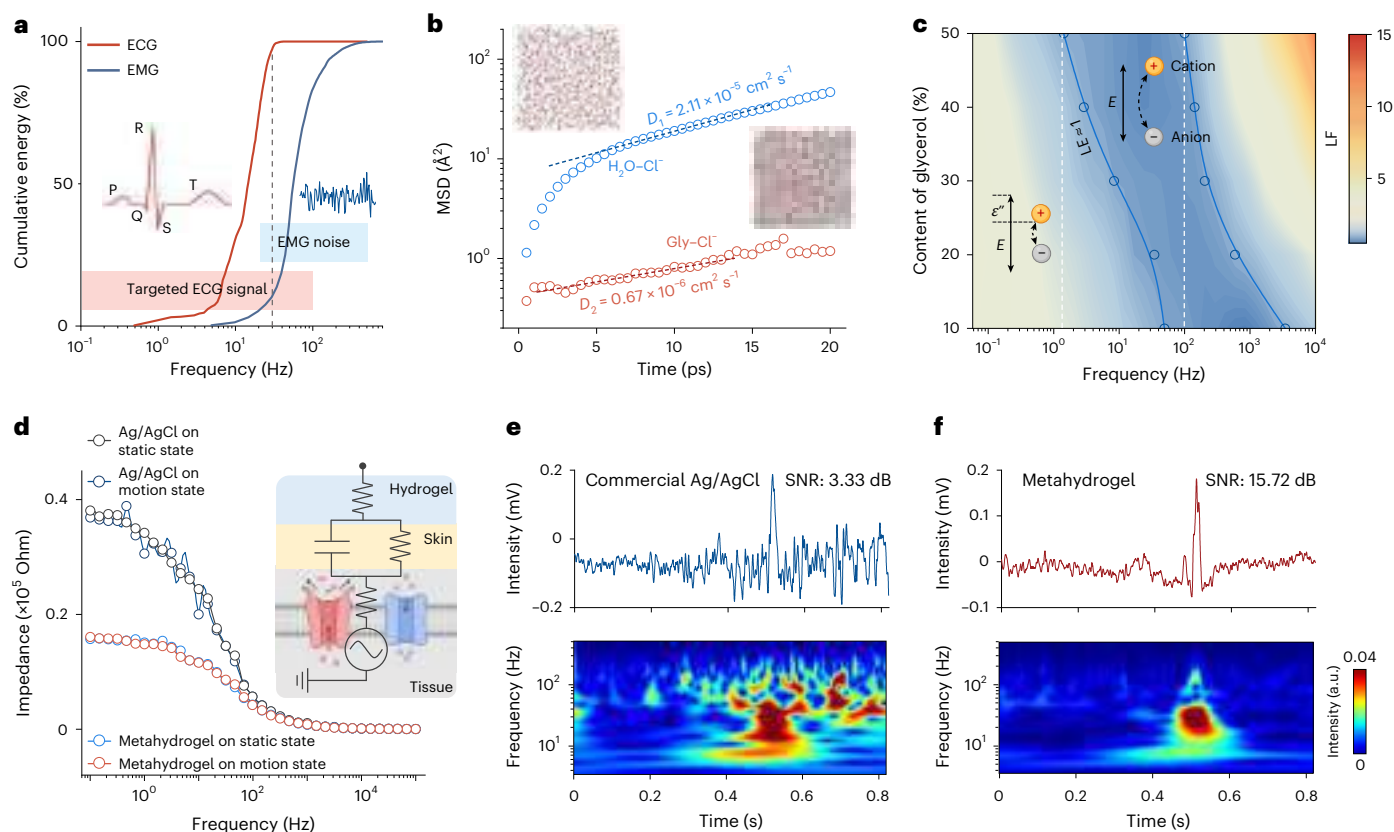


Fig. 3 | Frequency-selective ionic mobility by solvation structure design for mitigating for biopotential artefacts. **a**, Frequency-dependent cumulative energy spectra of ECG and EMG signals. The insets show their typical waveforms and peaks. **b**, Molecular dynamic simulation of solvation configuration and its MSD. **c**, Electrical loss spectrum versus frequency of hydrogel varying with glycerol contents. The inset presents the mobility response of ions under electric field. A loss factor (LF) greater than 1 indicates that ions cannot respond rapidly enough to the applied electric field. **d**, Evaluation of interfacial stability

between metahydrogel and commercial Ag/AgCl electrodes. The inset presents the equivalent circuit of the tissue–electrode interface. **e**, **f**, Comparison of single-period ECG signals with EMG noise collected by commercial Ag/AgCl electrode (**e**) and the metahydrogel (**f**). The bottom parts show the wavelet transform spectra, demonstrating that high-frequency noise is mitigated by the metahydrogel. Tissue schematic in **d** created in BioRender; Tian, G. <https://biorender.com/rj7b9v3> (2026).

and solvation molecules, as well as the overall size of the solvation structure³⁹. Optimizing the solvation structure of ionic hydrogel electrodes enables frequency-selective bioelectric sensing by regulating ion transport.

Given that CuCl_2 and K_2CrO_4 reactants were used to prepare the metastructure precipitation, the transport of K^+ and Cl^- predominantly determines the conductivity of hydrogel system. Hydroxyl-containing ($-\text{OH}$) molecules were introduced to modify the ion migration pathways, the energy landscape and the hydrogen-bond network within the electrolyte. Bonding energy analysis shows that increasing $-\text{OH}$ groups strengthens the binding energy (Supplementary Fig. 32), restricting solvation-shell reorientation and reducing ionic mobility. A biocompatible glycerol– H_2O mixed solvent was therefore selected to regulate ion transport behaviour. Incorporation of glycerol molecules reshapes the solvation-shell configuration and reduces the effective dielectric constant of the medium, strengthening ion–solvent interactions and limiting energetically assessable ion migration pathways. Molecular dynamic simulations confirmed reduced mean squared displacement (MSD) and diffusion coefficient with glycerol incorporation (Fig. 3b and Supplementary Fig. 33), consistent with experimental ionic diffusion measurements (Supplementary Fig. 34 and Supplementary Note 5). Control experiments using high-viscosity polyethylene oxide electrolytes showed uniform attenuation without frequency selectivity (Supplementary Fig. 35), demonstrating that viscosity alone does not account for the selective damping. Therefore, only solvents that

reshape the solvation shell and modulate ion–solvent interactions can effectively tune ionic relaxation dynamics.

Dielectric-loss spectra revealed that increasing glycerol content shifted the ionic response window towards lower frequencies (Fig. 3c). At high frequencies ($>100 \text{ Hz}$), delayed ionic relaxation caused conductive loss, whereas at low frequencies ($<1 \text{ Hz}$), sufficient ion migration leads to increased loss. Electrochemical impedance spectra further demonstrated a shift of the ionic relaxation peak to lower frequencies with increasing glycerol content (Supplementary Fig. 36). Optimizing the water-to-glycerol ratio (50:50 v/v) produced a response window of $\sim 1\text{--}100 \text{ Hz}$, matching ECG bandwidth while attenuating high-frequency EMG noise. Before practical application, we evaluated the interfacial impedance stability of the metahydrogel compared with a commercial Ag/AgCl electrode (Fig. 3d). The metahydrogel exhibits superior stability under dynamic conditions due to stable adhesion and the metastructural damping. Frequency sweep tests confirm selective signal transmission, whereas the Ag/AgCl electrode transmits electrical signals indiscriminately (Supplementary Fig. 37). Electrolyte-dependent transfer functions exhibit composition-dependent frequency shifts (Supplementary Fig. 38). When the glycerol content reaches 50%, the characteristic response frequency ($\sim 0.4\text{--}40 \text{ Hz}$) closely aligns with the ECG bandwidth. Under dynamic upper-limb motion, the Ag/AgCl electrode produced an SNR of 3.33 dB, while the metahydrogel achieved 15.72 dB (Fig. 3e and Supplementary Figs. 39 and 40).

Monitoring of the cardiovascular system in a dynamic environment

Having demonstrated the capability of our MAP in mitigating both mechanical and biopotential artefacts, we then explored its application in practical dynamic scenario. To assess the robustness of MAP, arterial pulse (AP) signals were analysed over a 10-min period (Supplementary Fig. 41). Without MAP, motion artefacts distorted waveforms and produced scattered Poincaré plots unsuitable for heart rate variability (HRV) analysis. By contrast, AP signals collected with MAP remained stable, yielding tightly clustered Poincaré plot and stable SBP and DBP waveforms (Fig. 4a and Supplementary Figs. 42 and 43), reflecting consistent autonomic nervous system regulation. ECG consistency relative to AP signals was assessed using Bland–Altman analysis, with 97.1% of data points within the 95% agreement limits (Fig. 4b and Supplementary Fig. 44), confirming MAP's reliability for physiological monitoring. Recurrence plots under dynamic motion showed large non-recurrent regions for the Ag/AgCl electrode, whereas MAP produced structured periodic patterns (Fig. 4c). Analysis of recurrence rate and determinism further confirms that MAP provides a clear representation of the autonomic nervous system activity (Supplementary Fig. 45), making it promising for fatigue assessment.

Although MAP effectively mitigates motion artefacts, residual physiological and unstructured interferences can still degrade signal quality⁷. Traditional filtering or smoothing algorithms indiscriminately remove noise, potentially discarding key physiological features. We therefore developed an autoencoder-based denoising algorithm designed to learn the structure of noise-free physiological signals (Supplementary Note 6), preserving critical features while suppressing artefactual signals (Fig. 4d, Extended Data Fig. 6 and Supplementary Fig. 46). The autoencoder alone increases the ECG SNR to 13.87 dB but fails to fully restore waveform features under severe motion-induced distortion (Supplementary Fig. 47). The metahydrogel alone improved the SNR to 15.75 dB, whereas combined processing reached 37.36 dB (Fig. 4e), demonstrating synergistic enhancement. This improved SNR substantially enhances feature peak identification, raising the detection accuracy from 52% to 93% for ECG waveforms.

To showcase the applicability of MAP in real-world dynamic environments, we monitored both ECG and BP signals from a moving participant, while simultaneously recording upper limb motion and acceleration using an attitude sensor (Supplementary Fig. 48). Despite strong motion artefacts, MAP combined with autoencoder processing effectively suppressed high-frequency EMG noise in the ECG spectrum (Fig. 4f). Similarly, BP measurements show improved agreement with a commercial sphygmomanometer, with absolute mean errors reduced from 2.02 to 0.27 and 3.45 to 0.37 mm Hg for DBP and SBP, respectively (Fig. 4g). Following the Institute of Electrical and Electronics Engineers (IEEE) standards for wearable electronics in BP monitoring, we benchmarked the accuracy of MAP against previously reported results^{40,41}. Most existing methods require measurements in a static state (grey region), whereas for kinetic conditions, our MAP combined with the denoising algorithm reduced standard deviation of DBP from 10.99 to 4.53 mm Hg (Fig. 4h), achieving comparable performance to that of a wearable ultrasound patch⁴² (3.90 mm Hg). Moreover, we benchmarked the performance of our device using a clinical ISO 81060-2 gold-standard protocol⁴³ (Supplementary Note 7 and Extended Data Fig. 7). MAP achieved mean errors of only 1.51/1.88 mm Hg for SBP/DBP with corresponding standard deviations of 2.99/2.86 mm Hg, well within the acceptance boundary. Overall, these results demonstrate the strong potential of MAP as a robust solution for haemodynamic monitoring in motion-intensive environments.

Demonstration of MAP's robustness in dynamic environments for daily fatigue profiling

To validate the robustness and practicality of MAP in real-world scenarios, a fully integrated, flexible and wearable MAP system was fabricated for

continuous, on-body physiological state monitoring during daily activities (Fig. 5a, Supplementary Fig. 49 and Supplementary Video 3). Commercial signal acquisition and wireless transmission modules enable arterial and electrophysiological signals transmission for processing (Supplementary Fig. 50). Frequency-dependent transfer-function analyses confirmed long-term stability of mechanical and electrical artefact mitigation (Supplementary Fig. 51). Moreover, controlled experiments were conducted on five participants, during which AP, BP and ECG signals were recorded under daily conditions. Comparisons of the coefficient of variation between MAP and commercial sensors demonstrated MAP's effective artefact mitigation (Fig. 5b). Fatigue levels for participants were simultaneously assessed using the fatigue assessment scale (FAS) questionnaire as a quasi-gold standard, with scores ranging from 10 to 50 points (Supplementary Note 8 and Supplementary Table 2). Given that the FAS is a unidimensional index, scores from 10 to 50 were interpreted as representing a progressive increase in fatigue⁴⁴.

Across participants, physiological signals show consistent fatigue-related trends during prolonged work without sufficient rest. Over the course of the day, short-term high intensity work or exercise increases energy consumption in the body and brain, triggering sympathetic nervous system (SNS) activation, thereby elevating heart rate (HR) and SBP⁴⁵. To assess autonomic nervous system dynamics, we extracted the low-frequency to high-frequency ratio (LF/HF) from ECG signals, which reflects the balance between SNS and parasympathetic nervous system (PNS) activity (Supplementary Fig. 52). Increased SNS activity suppresses the activation of PNS, which impacts cardiac homeostasis, resulting in a decreased HRV (Fig. 5c and Supplementary Fig. 53). Long-term monitoring accounted for circadian fluctuations, revealing fatigue-induced deviations beyond normal physiological ranges (Supplementary Fig. 54). Analysis of LF/HF ratio, sample entropy (SE) and the standard deviation of normal-to-normal intervals (SDNN) across participants revealed patterns indicating a disruption beyond normal physiological rhythm balance, reflecting pronounced PNS dysregulation (Fig. 5d and Supplementary Fig. 55). These results confirm the robustness of MAP to perform continuous, artefact-resilient physiological monitoring and reliable biomarker tracking.

Proof of application in data-driven fatigue profiling and extended scenarios

To demonstrate the potential of the MAP system for data-driven physiological analysis and preemptive intervention, we developed a prototype fatigue profiling framework as a proof-of-concept application. A deep learning pipeline was developed to extract physiological features and correlate them with questionnaire-based fatigue classifications. Principal component analysis was used for data dimensionality reduction and to identify the most discriminative ECG features (Extended Data Fig. 8 and Supplementary Figs. 56), which were used to train a convolutional neural network for multilevel fatigue classification (Supplementary Fig. 57). Feature space visualization using *t*-distributed stochastic neighbour embedding (*t*-SNE) revealed a clear clustering of fatigue states, achieving 92.0% classification accuracy, indicating that MAP provides high-quality data sufficient for capturing meaningful physiological variations (Supplementary Fig. 58).

We further explored the feasibility of fatigue level estimation using combined electrophysiological and haemodynamic features. Shapley additive explanation (SHAP) and permutation importance analyses confirmed the physiological interpretability of the learned features (Fig. 5e and Supplementary Fig. 59). A random forest regression model trained on FAS scores was constructed to assess fatigue levels with high confidence, achieving a coefficient of determination of 0.91 (Fig. 5f and Supplementary Fig. 60). Comparative analysis showed that MAP-enhanced classification achieved an area under the curve (AUC) of 0.93 in the receiver operating characteristic (ROC) analysis (Fig. 5g), substantially outperforming direct monitoring without MAP (AUC 0.64). These results demonstrated that the MAP-enabled signals retain

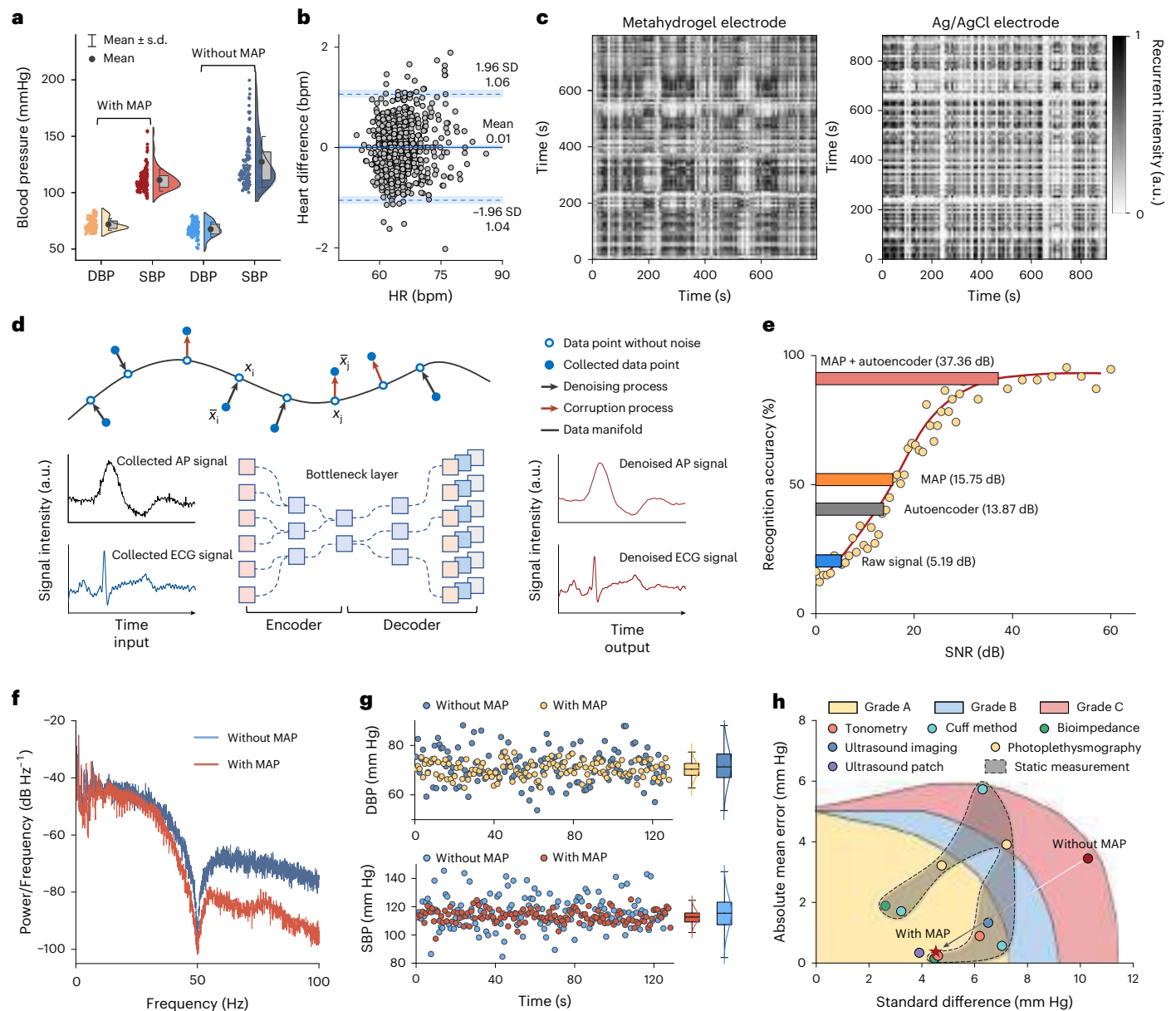


Fig. 4 | Demonstration of mechanical and biopotential artefacts mitigating by metahydrogel. **a**, Distribution of SBP and DBP data collected over 2 min under dynamic conditions with and without the use of metahydrogel. Data were obtained from one independent participant. The boxes represent the interquartile range (25th–75th percentile), while the whiskers indicate the mean \pm standard deviation (s.d.). **b**, Bland–Altman plot showing HR measurement agreement between the metahydrogel ECG electrode and piezoelectric artery sensor. **c**, Stability evaluation of collected BP signals by the recurrent analysis of collected ECG signals in time domain. **d**, Schematic of the autoencoder framework for denoising. The autoencoder model denoises the data by mapping measurement-corrupted data points back to the data manifold (black arrows). The bottom part presents typical AP and ECG signals before and after the denoising process. **e**, Calculated recognition accuracy of artery

pulse and ECG signal versus SNR. The bar plots show SNRs of sensing signals with different denoising process. **f**, Frequency–power spectra of ECG signals collected with and without the use of metahydrogel after processing with the autoencoder-based denoising algorithm. **g**, Stability evaluation of BP signals collected over 2 min during a kinetic activity. Data were obtained from one independent participant. Box plots show the median (central line), interquartile range (25th–75th percentile, box) and whiskers extending to the minimum and maximum values. **h**, Accuracy comparison of measured DBP achieved with and without metahydrogel (red star and red dot; the arrow serves as a guide to the eye) and other approaches. The grey region shows that these data were collected under static state, and the background shading indicates the IEEE accuracy categories (grades A, B and C) for wearable BP monitoring.

meaningful physiological information suitable for modelling fatigue-related trends. Expanded cohort validation shows strong agreement between predicted and subjective FAS scores (92.04%; Fig. 5h and Supplementary Fig. 61), supporting model robustness across individuals.

To further validate the applicability of the MAP, we extended its use to various physiological monitoring modalities, including heart sounds, breath sounds, voice, electroencephalography and electrooculogram signals (Supplementary Figs. 62–64). During signal acquisition, MAP

effectively suppressed diverse motion artefacts such as thoracic vibrations from breathing, laryngeal deformation during vocalization, and noise from body movements. By mitigating these artefacts, the system enables clearer and more accurate signal capture, facilitating more reliable disease diagnosis, speech recognition and brain activity sensing. These proof-of-concept demonstrations highlight the MAP system's capability to support artefact-free, multimodal physiological monitoring under realistic conditions, positioning the platform as a foundation

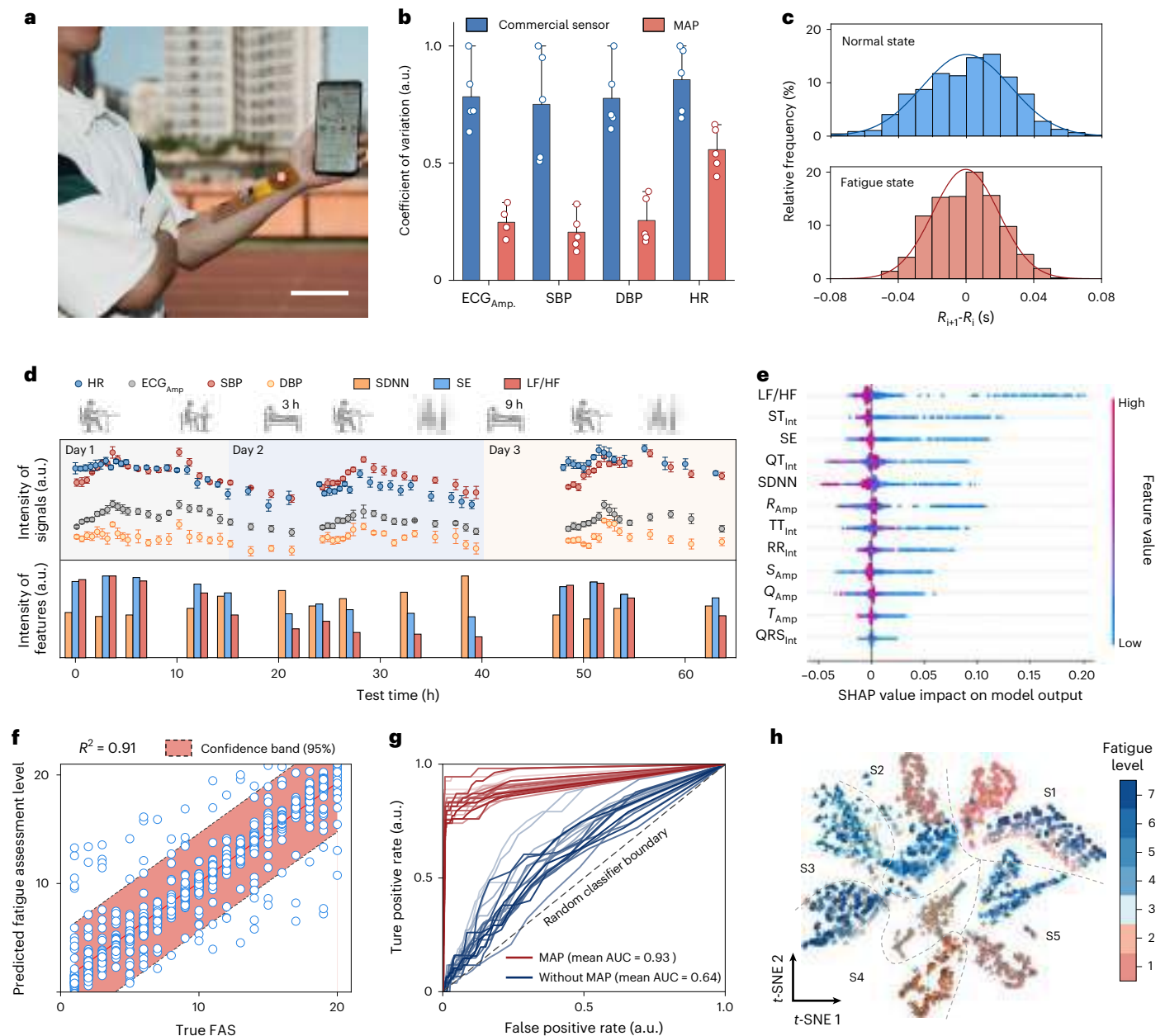


Fig. 5 | Artefact-free fatigue profiling in daily life. **a**, Photograph of a participant wearing the MAP for real-time physiological signals monitoring. The mobile phone shows the user interface. Scale bar, 10 cm. **b**, Robustness evaluation of collected different physiological signals from MAP and a commercial sensor. Data were obtained from independent participants ($n = 5$). Bars indicate mean \pm s.d. **c**, Frequency histogram of the difference of adjacent RR peaks ($R_{i+1}-R_i$) at normal and fatigue states. The narrower distribution indicates the reduced HRV. **d**, Continuous 3-day multimodal physiological signals monitoring during different daily activities on a participant. For each timepoint, and three segments within this window (over 2 min) were analysed. Error bars represent the mean \pm s.d. calculated from these replicates ($n = 3$).

e, SHAP summary plot for fatigue evaluation based on the dataset collected by the MAP. Each axis plots the distribution of SHAP value of the selected feature for predicted instance. **f**, True value versus assessed fatigue levels. Data are presented with a ± 2 -point buffer to account for potential errors in the FAS questionnaires. **g**, ROC curves evaluating the classification performance of the MAP system for fatigue state profiling. The curves are colour-coded from light to dark to represent increasing score scales on the fatigue assessment. **h**, t -SNE-based clustering of fatigue levels among different participants. A total of five participants were assessed, and their fatigue states were categorized into seven levels based on scores from the FAS. Activity icons in **d** created in BioRender; Tian, G. <https://biorender.com/omp1s6v> (2026).

for future large-scale, data-driven health analytics. Ultimately, the MAP system presents a promising framework for objective fatigue evaluation and real-time physiological monitoring in ambulatory settings and warrants broader validation across diverse populations and use cases.

Conclusions and outlook

We report a meta-topological hydrogel bioelectronic platform designed to enable high-fidelity, multisource, artefact-resilient physiological

signal acquisition in motion-intensive environments. By integrating phononic metastructure damping and ionic solvation engineering, this platform allows high-fidelity monitoring with targeted suppression of mechanical and biopotential artefacts, achieving low BP mean error of 0.37 and 0.27 mm Hg for SBP and DBP and high SNR of 37.36 dB for ECG in unstructured environments. To explore the feasibility of physiological pattern recognition, we conducted a proof-of-concept demonstration of fatigue profiling. By further processing these high-fidelity

multimodal physiological features using deep learning and regression models, fatigue levels could be evaluated with an accuracy exceeding 92.04%, demonstrating the platform's potential for early fatigue diagnosis and prevention. While fatigue monitoring serves as a representative application, we further validated the platform's robustness in other physiological monitoring tasks, with MAP shown to effectively mitigate motion-induced artefacts across multiple biosignal modalities. These results validate the feasibility of objective fatigue assessment and highlight MAP's utility in supporting data-driven health insights. Overall, this work establishes a versatile hydrogel interface for next-generation wearable bioelectronics, with wide-ranging applicability in real-world settings. This platform lays the groundwork for future advances in continuous, artefact-resilient biosensing and intelligent physiological monitoring, paving the way for personalized digital and connected healthcare.

Methods

All testing involving human participants was approved by the institutional review board of Southwest Jiaotong University (reference no. SWJTU-23012-NSFC(133)).

Acrylamide (AAM) monomer (>98% purity) was purchased from Tokyo Chemical Industry. *N,N'*-methylene(bis)acrylamide (MBAA), potassium peroxydisulfate (KPS), *N,N,N',N'*-tetramethylene-diamine (TEMED), copper chloride (CuCl_2) and gelatin (porcine skin, gel strength 300) were purchased from Sigma-Aldrich. Potassium chromate (K_2CrO_4 , >99.0% purity) was purchased from Alfa Aesar. Agarose powder (biotechnology grade with a low electroendosmosis) was purchased from Axil Scientific. PDMS (Sylgard 184) and its crosslinker were purchased from Dow Corning. The sources of commercial damper materials are as follows: Alpha-gel (GT-4, Taica), plasticine (Plasticine-200, Seow Khim Polythelene), D30 (D30-Elbow, D30) and starch (Sigma-Aldrich). Unless otherwise specified, all chemicals were used without further purification.

Fabrication

Preparation of metahydrogel. The PAAm hydrogel precursor was prepared by dissolving 1.446 g of AAm monomer and 0.016 g of MBAA in 9.2 ml deionized water with vigorous stirring for 10 min. Air bubbles in the solution were removed by vacuum degassing. Then, 0.02 g of KPS and 0.04 g of K_2CrO_4 were carefully added without introducing additional oxygen. Afterwards, 20 μl of TEMED was immediately added, and the mixture was stirred in an ice bath for 5 min to ensure uniform mixing. The resulting precursor was poured into an acrylic mould ($5 \times 5 \times 0.2 \text{ cm}^3$), and placed in an oven at 60 °C for 2 h to conduct prepolymerization, with the mould covered to prevent solvent evaporation. This was followed by a secondary polymerization at room temperature for 4 h, during which saturated KCl solution was used to maintain a relative humidity above 80%. For preparing the outer CuCl_2 source, 1.8 g of agarose was first dissolved in 28.2 ml deionized water by stirring at 90 °C, and the solution was then poured into a cylindrical acrylic mould (diameter 1.0 cm, height 2.5 cm) and placed in a refrigerator to solidify (4 °C, 20 min). The solidified agarose stamp was then immersed in 1 M CuCl_2 solution for 40 min to absorb the electrolyte. The agarose stamp was placed at the centre of the PAAm hydrogel, allowing CuCrO_4 precipitate to gradually form through ion diffusion and reaction in the following 48 h. The morphology of the resulting metastructure was controlled by adjusting the crosslinking density of the PAAm hydrogel and the placement of the agarose stamp. The preparation of other metastructural pattern systems is detailed in Supplementary Note 3. To modulate the hydrophobic properties of the metahydrogel surface, it was treated using fluorine plasma. First, the metahydrogel was freeze-dried to remove moisture, and then placed in an inductively coupled plasma etching system (DICS-ICP-601, Chuangshi Weina Technology) for treatment. The working gas was CHF_3 , with a chamber pressure of 2 Pa, a source power of 200 W and a bias power of 100 W.

Preparation of other damping materials. The reference PDMS elastomer was prepared by mixing the base and curing agent at a mass ratio of 20:1. After thorough mechanical stirring, the mixture was degassed and poured into a mould, then cured at 80 °C for 4 h. For the starch damper sample, a 55 wt% starch aqueous solution was prepared and poured into a cylindrical mould. The mould was sealed on both sides using polyurethane films to facilitate subsequent damping tests. For the plasticine sample, 5 wt% of water was added and mixed thoroughly, and the material was then shaped into cylindrical forms for testing.

Fabrication of sensing devices and integrated wireless systems.

Platinum wire was used as the electrode for the metahydrogel, effectively preventing ionic corrosion and electrochemical reactions at the electrode–hydrogel interface. A piezoelectric polymer film sensor was attached to the hydrogel matrix for pulse signal monitoring. The entire wireless signal acquisition system was fabricated on a flexible printed circuit board, integrating a Bluetooth-enabled microcontroller (ESP32 WROOM 32), a piezoelectric signal acquisition and amplification module, a power supply module, an ECG acquisition module (AD8232) and a serial communication module. The connections among different components are presented in Supplementary Fig. 50. The key data-acquisition parameters of the integrated system are summarized as follows. ECG and AP signals are sampled at a rate of 500 Hz using a 12-bit analog-to-digital converter (ADC) embedded in the microcontroller, and the ECG acquisition module operated under a fixed gain of 100. Considering that the metahydrogel damper inherently suppresses mechanical and biopotential artefacts above 1 Hz, a hardware high-pass cut-off was implemented in the acquisition circuit to stabilize the baseline without interfering with the damping behaviours of hydrogel, and a 50-Hz notch filter was used to remove power-line interference. All raw data were recorded without compression to preserve signal integrity. To ensure precise temporal alignment across ECG and artery pulse channels, a time stamp was implemented based on the ESP32 system clock, and all acquisition modules were synchronized through a shared microcontroller-triggered signal.

Characterizations

Materials characterization. The morphology and EDS mapping of metahydrogel were characterized by field-emission scanning electron microscopy (JSM-7001F, JEOL). The hydrogel sample was prepared via freeze-drying to prevent the collapse of the porous structure. The optical photographs of surficial and cross-sectional morphologies of metahydrogel were taken and recorded via an optical microscope (BX53M, Olympus). The Raman mapping of CuCrO_4 was collected via a Raman imaging microscope (Alpha 300R, WITec, Oxford Instruments) with a 532-nm laser at 2 mW power. The spatial resolution of the chemical mapping was 10 μm . The modulus of metahydrogel was measured by a universal testing machine (MultiTest 1, Mecmesin) at room temperature, where the tensile/compression rate was set as 50 mm min^{-1} . The electrochemical properties of metahydrogel were measured by an electrochemical workstation (CHI660E, Chenhua Device Company), and the sample was fully swollen in the electrolyte solution before testing. The conductivity and viscosity of different solutions were measured by a conductivity meter (Seven Compact, Mettler Toledo) and an Ubbelohde viscometer, respectively.

Damping performance tests. Dynamic mechanical testing was performed by a rheometer (MCR 302, Anton Paar RheoCompass) using a measuring plate with a diameter of 20 mm; the frequency was swept from 100 to 0.1 Hz at room temperature. For testing the propagation of mechanical waves in the samples, a full-field laser scanning vibrometer was used (LV-SC400, Sunny Optical Technology). A vibration motor was fixed at one end of the sample, and a function generator was used to drive the vibration source. The laser system then scanned

designated areas on the sample to measure the vibration response. To ensure measurement accuracy, a layer of reflective metallic particles was sprayed onto the sample surface to improve laser reflectivity. For the omnidirectional interference resistance test, the samples were fixed in a designed testing mould, with a piezoelectric sensor placed below it. A constant vertical force was applied to the sample using a tensile testing machine. During the test, disturbance forces were applied from various angles through the outer frame of the mould (illustrated in Fig. 2g). By comparing the force signals received by the piezoelectric sensor with the applied forces, the interference-resistance performance of the hydrogel was evaluated. The SNR of transmitted mechanical signals was obtained using the same set-up. The electrical damping performance was evaluated using a broadband dielectric spectroscopy (Concept 80, Novocontrol). Before testing, the sample surface was dried with nitrogen gas to eliminate the influence of surface water. During the test, a 1-V a.c. voltage was applied, and the frequency was swept from 10^{-2} Hz to 10^4 Hz. All measurements were conducted at room temperature.

Cell cytotoxic test. The fibroblast cell line (L929) served as the model to evaluate in vitro cytotoxicity of the metahydrogel. Cells were purchased from ATCC and authenticated by the supplier through quality control testing. The prepared metahydrogel and reference samples were immersed in a phosphate-buffered saline–penicillin mixture. After incubation for a specified time, the extraction media were collected and applied to cell culture wells for an additional 24 h of incubation. Subsequently, the cell activity was evaluated using the Cell Counting Kit-8 assay. In parallel, a live/dead staining assay was performed to evaluate cell proliferation. The cell seeding and culture procedure were the same as described above. On days 1 and 3 of coculture, the cells were washed with phosphate-buffered saline and stained using a Calcein-AM/PI double staining kit. The cells were then observed under a fluorescence microscope. Live cells emitted green fluorescence, while dead cells showed red fluorescence.

Performance test and application validation of the MAP

Reliability evaluation of collected BP signals. To evaluate the reliability of the MAP in BP monitoring, we used a commercial photoplethysmography device as a reference. Given that commercial devices are susceptible to motion artefacts, the referenced BP results were collected under resting conditions, with different methods performed sequentially within a short timeframe to minimize the influence of physiological fluctuations. During BP signal acquisition with or without the MAP system, only hand movements were introduced to simulate motion artefacts, while avoiding full-body motion to prevent systemic physiological changes. The acquired arterial piezoelectric pulse signals were converted into BP waveforms using the method described in Supplementary Note 4. These waveforms were subsequently calibrated, enabling accurate and continuous BP monitoring under motion conditions.

Physiological signal acquisition in daily-life environments. The developed flexible wearable system (Fig. 5a) was utilized for physiological signal acquisition under daily-life environment. The pressure sensor and hydrogel electrode were used to collect BP and ECG signals, respectively. The signals were processed by dedicated acquisition modules and wirelessly transmitted via Bluetooth to a mobile phone or computer terminal for visualization and subsequent analysis. For consistency, light and routine signal preprocessing was applied to the collected data, as the metahydrogel already performs the primary artefact suppression. Artery pulses obtained from the piezoelectric sensor were gently smoothed using a Savitzky–Golay filter (window length 5) without altering their intrinsic amplitude and morphology. All preprocessing procedures were intentionally kept simple and processed in software to maintain consistency and reproducibility across

datasets. During motion-state monitoring, a commercial posture sensor was attached to the participant's arm to synchronously record physical activity data. For long-term monitoring, to reduce data volume and processing complexity, the sampling interval was set to once every 30 min, with each sampling lasting for 2 min. The physiological metrics were calculated as the average values over each sampling period. To simulate fatigue conditions as realistically as possible, participants are required to engage in prolonged and high-intensity simulated driving games. Meanwhile, a fatigue assessment questionnaire was administered to evaluate and confirm the participant's fatigue state.

Theoretical simulation

Simulation of metastructure filtering. The metahydrogel consists of a soft matrix embedded with periodic structures formed by nanoparticle precipitation. These rigid nanoparticle–soft matrix units act as local resonators, absorbing mechanical energy at specific frequencies. For pressure (P) fluctuations in the matrix, the mechanical wave propagation follows the scalar wave equation:

$$\nabla^2 P - \frac{1}{c^2} \frac{\partial^2 P}{\partial t^2} = 0,$$

where $c = \sqrt{K/\rho}$ is the wave velocity determined by the effective medium modulus (K) and mass density (ρ). The local resonator can be approximated as a mass–spring system

$$m\ddot{x} + c\dot{x} + kx = F_0 e^{i\omega t},$$

where m is the effective mass of the nanoparticle cluster, and k is the elastic stiffness of the surrounding hydrogel. Resonance damping occurs near the natural frequency $\omega_0 = \sqrt{k/m}$, where the absorbed energy is maximized. The given mechanical wave inputs were applied to evaluate the wave transmission and damping performance of the metastructural hydrogel.

Simulation of solvation structure based on molecular dynamics.

Molecular dynamics were performed to investigate the structural and dynamic behaviour of the solvation system in Materials Studio 2022 software (Accelrys Software), using the Forcite module with the ab-initio-optimized COMPASS III force field. Molecular models were first constructed and subjected to geometry optimization to mitigate unfavourable conformations, and the canonical ensemble (N, V, T) simulations were carried out under periodic boundary conditions to mimic bulk-like conditions. The timestep was set to 1.0 fs, and the non-bonded interaction cut-off distance was set to 1.25 nm. The MSD of molecules was calculated as a function of time to analyse molecular mobility, and the diffusion coefficient (D) of molecules was obtained through the Einstein relation

$$D = \lim_{t \rightarrow \infty} \frac{\langle r^2(t) \rangle}{6t},$$

where $m = 6$ for three-dimensional cases, and r^2 is the ensemble-averaged MSD. The radial distribution function $g(r)$ was computed to quantify the probability of finding a given solvation pair at specific radial distance, offering insight into short-range ordering and solvation-shell structures. The binding energy (E_{bind}) between ion and solvent was calculated to evaluate the interaction strength as

$$E_{\text{bind}} = E_{\text{total}} - (E_{\text{ion}} + E_{\text{solvent}}),$$

where E_{total} is the energy of optimized solvation complex, and E_{ion} and E_{solvent} are the energies of the isolated ion and solvent in the same environment, respectively. All simulation and analyses were conducted using default convergence criteria in Materials Studio.

Data processing and analysis

Concordance analysis of BP signals. The four-quadrant plot was constructed to assess the accuracy of SBP and DBP signals collected by different sensing systems (Fig. 2h). The horizontal and vertical axes represent the measurement difference and reference difference, respectively. The data points located in the first and third quadrants indicate consistent trends between the measured and reference BP. The concordance rate (CR) is calculated as

$$\text{CR} = \frac{N_{Q1} + N_{Q3}}{N_{\text{Total}}} \times 100\%,$$

where N_{Q1} and N_{Q3} are the number of points in the first and third quadrants, respectively, and N_{Total} is the total number of data points. To minimize the influence of measurement noise and physiological fluctuations, an exclusion zone of ± 3 mm Hg was introduced in this analysis.

Recurrence analysis for ECG signal stability evaluation. The recurrence intensity mapping was performed to estimate the stability and dynamics evolution of ECG signals with different monitoring systems. For the collected ECG time series $x(i)$, the phase space is reconstructed using time-delay embedding:

$$X(i) = [x(i), x(i + \tau), x(i + 2\tau), \dots, x(i + (m - 1)\tau)],$$

where τ is the time delay and m is the embedding dimension. The similarity between any two-phase space vectors $X(i)$ and $X(j)$ was then computed on the basis of their Euclidean distance:

$$D_{ij} = \|X(i) - X(j)\|.$$

To improve interpretability, the distance D_{ij} was normalized and transformed into a recurrence intensity matrix (Fig. 4c), where colour gradients represent the similarity between different timepoints.

SNR analysis in the frequency domain of ECG signal. The power spectral density was conducted to estimate the SNR of ECG signal (Fig. 4f), the SNR at each frequency (f) was calculated as

$$\text{SNR}(f) = 10 \log_{10} \left(\frac{P_{\text{signal}}(f)}{P_{\text{noise}}(f)} \right) \text{ (dB)}.$$

This analysis allows a frequency-resolved assessment of signal quality, facilitating direct comparison between different sensing systems.

Classification accuracy assessment based on ROC. To assess the effectiveness and accuracy of fatigue evaluation, a comparative ROC analysis using two datasets: one collected with the MAP and the other collected without MAP. The extracted features were trained with a random forest classifier to predict subjective fatigue scales, which served as ground truth. ROC curves were generated by plotting the true positive rate (sensitivity) against the false positive rate ($1 - \text{specificity}$) across a range of classification thresholds. The AUC was calculated to quantify the discriminative power of each method.

Statistics and reproducibility

All statistical analyses were performed using OriginPro (version 2024; OriginLab) and MATLAB (R2022a). Detailed statistical methods and analysis procedures are described in the corresponding figure legends and Methods sections.

Reporting summary

Further information on research design is available in the Nature Portfolio Reporting Summary linked to this article.

Data availability

The data supporting the findings of this study are available within the Article and its Supplementary Information. Source data are provided with this paper.

Code availability

The code used to visualize the ion kinetic diffusion and to extract and analyse the physiological features is available via GitHub at <https://github.com/TianGuoN/Metahydrogel>.

References

- Zhou, S., Park, G., Lin, M., Yang, X. & Xu, S. Wearable ultrasound technology. *Nat. Rev. Bioeng.* <https://doi.org/10.1038/s44222-025-00329-y> (2025).
- Kim, J., Campbell, A. S., de Avila, B. E. & Wang, J. Wearable biosensors for healthcare monitoring. *Nat. Biotechnol.* **37**, 389–406 (2019).
- Min, S. et al. Wearable blood pressure sensors for cardiovascular monitoring and machine learning algorithms for blood pressure estimation. *Nat. Rev. Cardiol.* <https://doi.org/10.1038/s41569-025-01127-0> (2025).
- Xu, C., Solomon, S. A. & Gao, W. Artificial intelligence-powered electronic skin. *Nat. Mach. Intell.* **5**, 1344–1355 (2023).
- Deng, W. L. et al. Piezoelectric nanogenerators for personalized healthcare. *Chem. Soc. Rev.* **51**, 3380–3435 (2022).
- Tian, G. et al. A wearable all-in-one obstructive sleep apnea management system with flexible piezoelectric monitoring and soft magnetoelastic stimulating. *Matter* <https://doi.org/10.1016/j.matt.2025.102323> (2025).
- Park, B., Jeong, C., Ok, J. & Kim, T. I. Materials and structural designs toward motion artifact-free bioelectronics. *Chem. Rev.* **124**, 6148–6197 (2024).
- Yin, J., Wang, S., Tat, T. & Chen, J. Motion artefact management for soft bioelectronics. *Nat. Rev. Bioeng.* **2**, 541–558 (2024).
- Liu, S., Rao, Y., Jang, H., Tan, P. & Lu, N. Strategies for body-conformable electronics. *Matter* **5**, 1104–1136 (2022).
- Wang, G. K., Yang, Y. M. & Jia, D. Programming viscoelastic properties in a complexation gel composite by utilizing entropy-driven topologically frustrated dynamical state. *Nat. Commun.* **15**, 3569 (2024).
- Luo, J. et al. A selective frequency damping and Janus adhesive hydrogel as bioelectronic interfaces for clinical trials. *Nat. Commun.* **15**, 8478 (2024).
- Kim, D. H. et al. Epidermal electronics. *Science* **333**, 838–843 (2011).
- Wang, W. et al. Strain-insensitive intrinsically stretchable transistors and circuits. *Nat. Electron.* **4**, 143–150 (2021).
- Franklin, D. et al. Synchronized wearables for the detection of haemodynamic states via electrocardiography and multispectral photoplethysmography. *Nat. Biomed. Eng.* **7**, 1229–1241 (2023).
- Zhao, X. et al. A self-filtering liquid acoustic sensor for voice recognition. *Nat. Electron.* **7**, 924–932 (2024).
- Zhang, J., Liu, Y. & Wu, P. An elastic piezoelectric nanomembrane with double noise reduction for high-quality bandpass acoustics. *Nat. Commun.* **15**, 8920 (2024).
- Xu, Z. et al. Rapidly damping hydrogels engineered through molecular friction. *Nat. Commun.* **15**, 4895 (2024).
- Shen, S., Du, Z., Zhou, P., Zou, Z. & Lyu, X. A mechanically robust, damping, and high-temperature tolerant ion-conductive elastomer for noise-free flexible electronics. *Adv. Funct. Mater.* **34**, 2408017 (2024).
- Reiling, J. The 'Day of Rest' and human efficiency. *J. Am. Med. Assoc.* **62**, 1810 (1914).
- Fukuda, K. et al. The chronic fatigue syndrome: a comprehensive approach to its definition and study. *Ann. Intern. Med.* **121**, 953–959 (1994).

21. Aaronson, L. S. et al. Defining and measuring fatigue. *Image J. Nurs. Sch.* **31**, 45–50 (1999).
22. QuickStats: percentage of adults aged ≥ 18 years who felt very tired or exhausted most days or every day in the past 3 months, by sex and age group. National Health Interview Survey, United States. *Morb. Mortal. Wkly. Rep.* **72**, 1248 (2023).
23. Swain, M. G. Fatigue in chronic disease. *Clin. Sci.* **99**, 1–8 (2000).
24. Kaveh, R., Schwendeman, C., Pu, L., Arias, A. C. & Muller, R. Wireless ear EEG to monitor drowsiness. *Nat. Commun.* **15**, 6520 (2024).
25. Xu, C. et al. A physicochemical-sensing electronic skin for stress response monitoring. *Nat. Electron.* **7**, 168–179 (2024).
26. Mahato, K. et al. Hybrid multimodal wearable sensors for comprehensive health monitoring. *Nat. Electron.* **7**, 735–750 (2024).
27. Mu, S., Liao, S., Tao, K. & Shen, Y. Intelligent fatigue detection based on hierarchical multi-scale ECG representations and HRV measures. *Biomed. Signal Process. Control* **92**, 106127 (2024).
28. Lu, K., Dahlman, A. S., Karlsson, J. & Candefjord, S. Detecting driver fatigue using heart rate variability: a systematic review. *Accid. Anal. Prev.* **178**, 106830 (2022).
29. Zeng, Q. et al. A digitally embroidered metamaterial biosensor for kinetic environments. *Nat. Electron.* **7**, 1025–1034 (2024).
30. Adão Martins, N. R., Annenheim, S., Spengler, C. M. & Rossi, R. M. Fatigue monitoring through wearables: A state-of-the-art review. *Front. Physiol.* **12**, 790292 (2021).
31. Liu, Z. et al. Locally resonant sonic materials. *Science* **289**, 1734–1736 (2000).
32. Sigmund, O. & Jensen, J. S. Systematic design of phononic band-gap materials and structures by topology optimization. *Philos. Trans. R. Soc. Lond. Ser. A* **361**, 1001–1019 (2003).
33. Unwin, A. P. et al. Escaping the Ashby limit for mechanical damping/stiffness trade-off using a constrained high internal friction interfacial layer. *Sci. Rep.* **8**, 2454 (2018).
34. Dai, Y. et al. Soft hydrogel semiconductors with augmented biointeractive functions. *Science* **386**, 431–439 (2024).
35. Park, S. J. & Tamura, T. Distribution of evaporation rate on human body surface. *Ann. Physiol. Anthropol.* **11**, 593–609 (1992).
36. van de Vosse, F. N. & Stergiopoulos, N. Pulse wave propagation in the arterial tree. *Annu. Rev. Fluid Mech.* **43**, 467–499 (2011).
37. Tian, G. et al. Hierarchical piezoelectric composites for noninvasive continuous cardiovascular monitoring. *Adv. Mater.* **36**, 2313612 (2024).
38. Chen, X., Lin, J., Huang, C. & He, L. A novel method based on adaptive periodic segment matrix and singular value decomposition for removing EMG artifact in ECG signal. *Biomed. Signal Process. Control* **62**, 102060 (2020).
39. Lu, D. et al. Ligand-channel-enabled ultrafast Li-ion conduction. *Nature* **627**, 101–107 (2024).
40. *IEEE Standard for Wearable, Cuffless Blood Pressure Measuring Devices—Amendment 1 1708a-2019* 1–35 (IEEE Standard Association, 2019).
41. Kireev, D. et al. Continuous cuffless monitoring of arterial blood pressure via graphene bioimpedance tattoos. *Nat. Nanotechnol.* **17**, 864–870 (2022).
42. Zhou, S. et al. Clinical validation of a wearable ultrasound sensor of blood pressure. *Nat. Biomed. Eng.* **9**, 865–881 (2025).
43. *ISO 81060-2:2018, Non-invasive Sphygmomanometers. Part 2: Clinical Investigation of Intermittent Automated Measurement Type* edn 3, 1–36 (ISO, 2018).
44. Michielsen, H. J., De Vries, J. & Van Heck, G. L. Psychometric qualities of a brief self-rated fatigue measure: The Fatigue Assessment Scale. *J. Psychosom. Res.* **54**, 345–352 (2003).
45. Freeman, J. V., Dewey, F. E., Hadley, D. M., Myers, J. & Froelicher, V. F. Autonomic nervous system interaction with the cardiovascular system during exercise. *Prog. Cardiovasc. Dis.* **48**, 342–362 (2006).

Acknowledgements

This research is supported by Agency for Science, Technology and Research (A*STAR), under its RIE2025 Manufacturing, Trade and Connectivity (MTC) award Individual Research Grant (IRG award M22K2c0081, G.W.H.), the Ministry of Education, Singapore, under the Academic Research Fund Tier 1 (FY2023, A-8002151-00-00, G.W.H.) and NUS research support (A-8003994-00-00, G.W.H.). G.T. gratefully acknowledges financial support from China Scholarship Council. We thank M. J. Wong from Hwa Chong Institution, as well as X. Li and Y. Liu from Southwest Jiaotong University, for their contributions to data collection and materials preparation.

Author contributions

G.W.H., W.G., W.Y. and G.T. conceived the proposal and designed the projects. G.T., L.H. and W.D. designed the materials system and conducted overall experiments. G.T., X.P. and Z.L. designed the device structure. L.H., W.L. and W.L.O. performed the materials characterization and application data collection. Y.S. assisted in the materials preparation and device characterization. G.T. and C.L. designed the circuit and conducted the simulation. Y.Z. organized the participant study. G.T., G.W.H., W.G., W.Y. and W.D. wrote the original manuscript. All authors discussed the results and commented on the manuscript.

Competing interests

The authors declare no competing interests.

Additional information

Extended data is available for this paper at <https://doi.org/10.1038/s44460-026-00055-x>.

Supplementary information The online version contains supplementary material available at <https://doi.org/10.1038/s44460-026-00055-x>.

Correspondence and requests for materials should be addressed to Weiqing Yang, Wei Gao or Ghim Wei Ho.

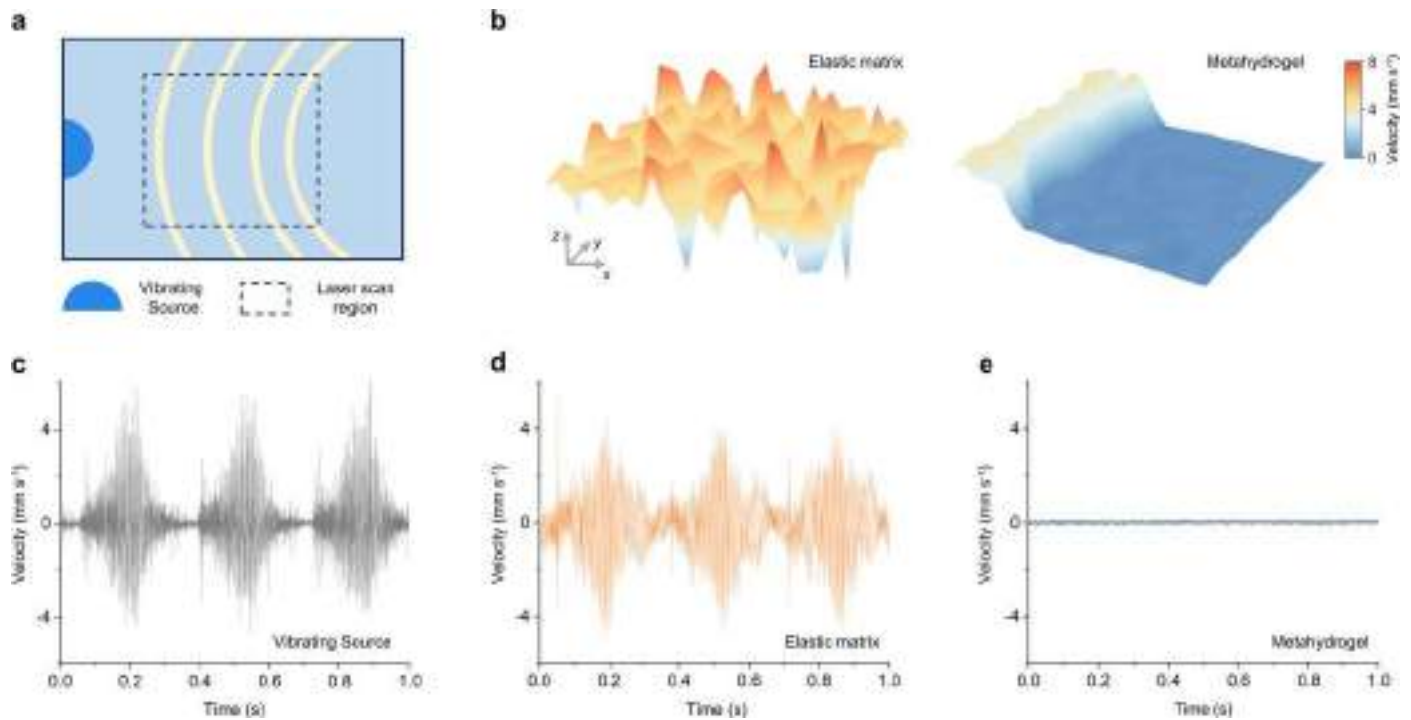
Peer review information *Nature Sensors* thanks Wubin Bai, Yuanwen Jiang and the other, anonymous, reviewer(s) for their contribution to the peer review of this work.

Reprints and permissions information is available at www.nature.com/reprints.

Publisher's note Springer Nature remains neutral with regard to jurisdictional claims in published maps and institutional affiliations.

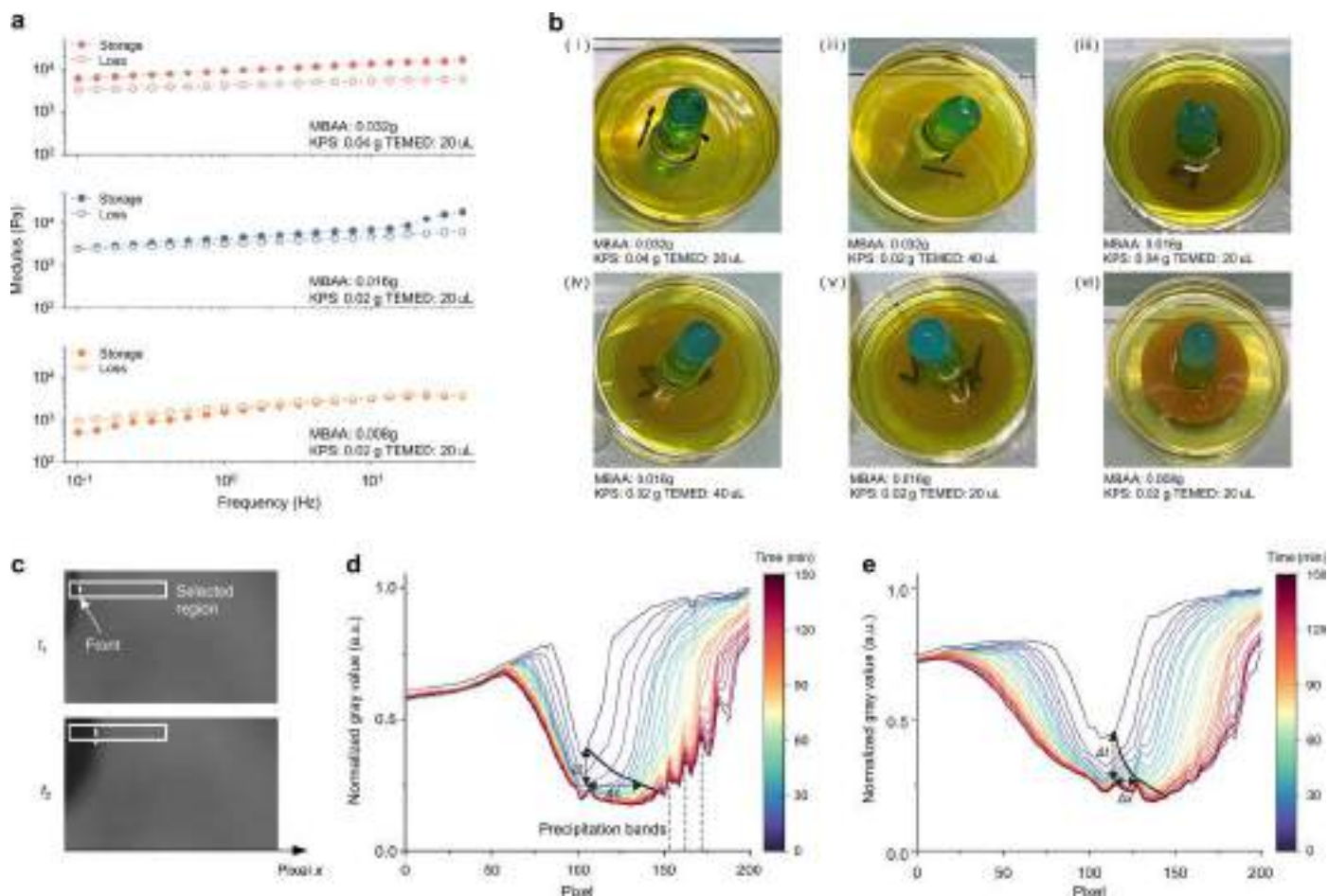
Open Access This article is licensed under a Creative Commons Attribution-NonCommercial-NoDerivatives 4.0 International License, which permits any non-commercial use, sharing, distribution and reproduction in any medium or format, as long as you give appropriate credit to the original author(s) and the source, provide a link to the Creative Commons licence, and indicate if you modified the licensed material. You do not have permission under this licence to share adapted material derived from this article or parts of it. The images or other third party material in this article are included in the article's Creative Commons licence, unless indicated otherwise in a credit line to the material. If material is not included in the article's Creative Commons licence and your intended use is not permitted by statutory regulation or exceeds the permitted use, you will need to obtain permission directly from the copyright holder. To view a copy of this licence, visit <http://creativecommons.org/licenses/by-nc-nd/4.0/>.

© The Author(s) 2026



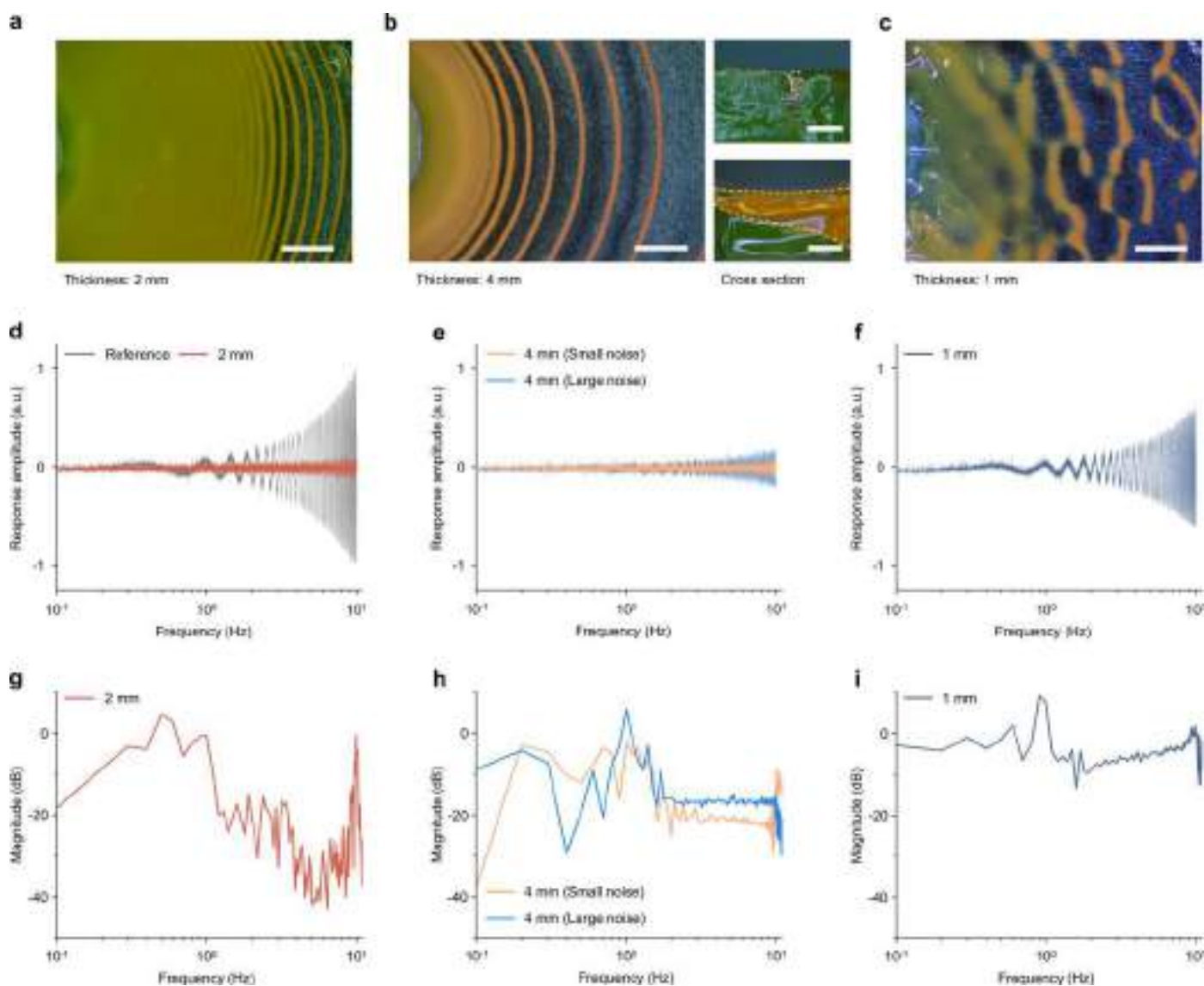
Extended Data Fig. 1 | Evaluation of vibration transmission across different materials systems. **a**, Schematic of the vibration wave propagation test. A vibration source is fixed at one end of the sample to generate mechanical waves. The laser Doppler vibrometer was used to scan and measure the vibration

response in selected regions. **b**, Distribution of vibrating velocity for elastic matrix and metahydrogel damper, the precipitation pattern in hydrogel blocks propagation of mechanical wave. **c–e**, Extracted vibrating velocity at selected single point from the source (**c**), elastic matrix (**d**) and metahydrogel (**e**).



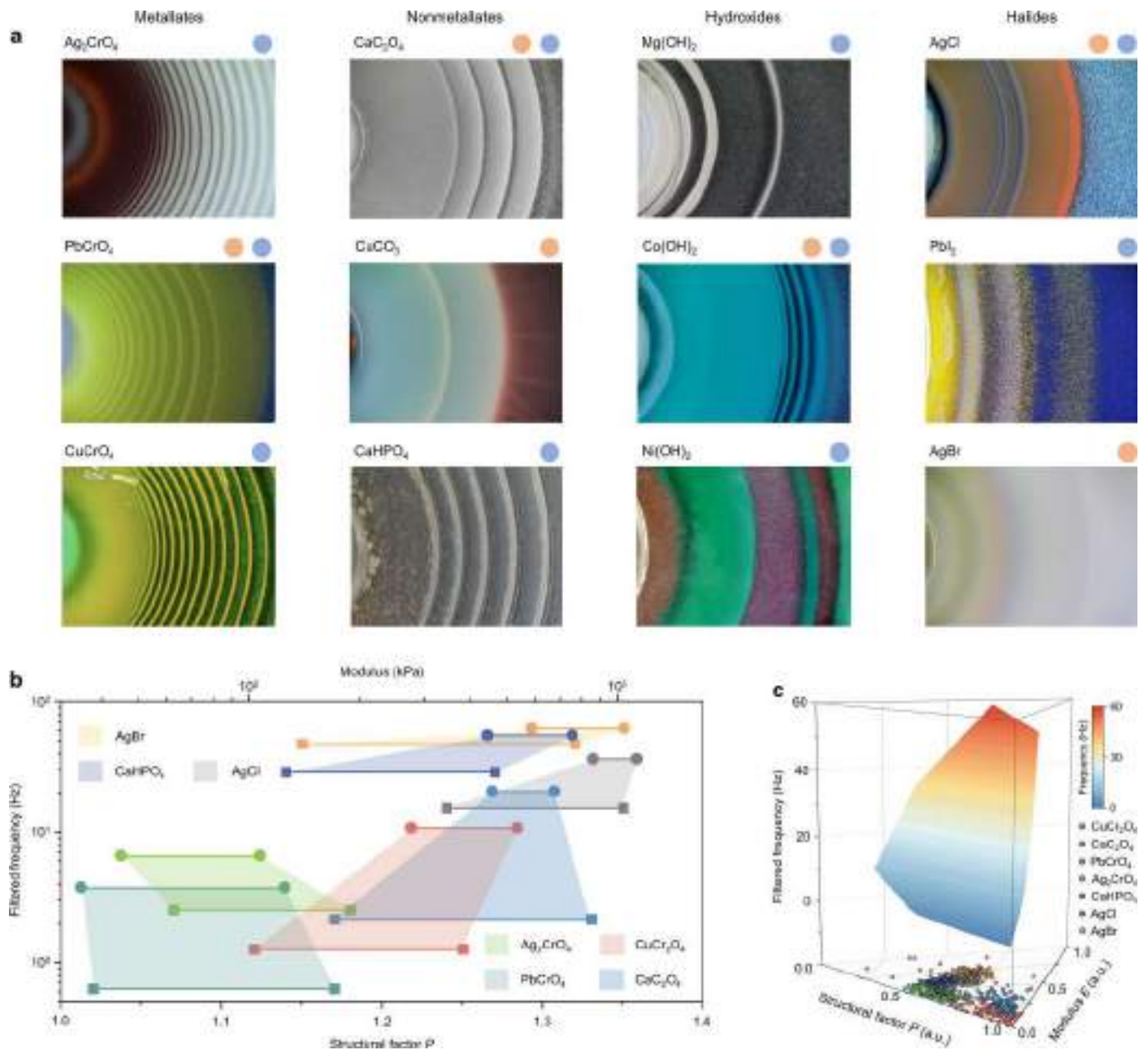
Extended Data Fig. 2 | Different precipitation patterns modulated by precursor rheology, gelation rate, crosslinking, and ion reaction-diffusion rate. **a**, Rheological properties of the hydrogel precursors prepared under different reaction parameters. **b**, Optical images of the final precipitation patterns formed in hydrogels prepared with different reaction parameters. **c**, Optical images showing the migration of the reaction front driven by ion diffusion. **d-e**, Time-dependent grayscale profiles extracted from real-time

pictures as presented in (c) under different reaction parameters (**d**: MBAA: 0.016 g, KPS: 0.02 g, TEMED: 20 μ L; **e**: MBAA: 0.032 g, KPS: 0.02 g, TEMED: 40 μ L). The position of the reaction front is indicated by the marked black lines, the ratio of front displacement to time provides an approximate measurement of ion diffusion rate. Samples with higher crosslinking density and faster gelation exhibit slower reaction-diffusion kinetics.



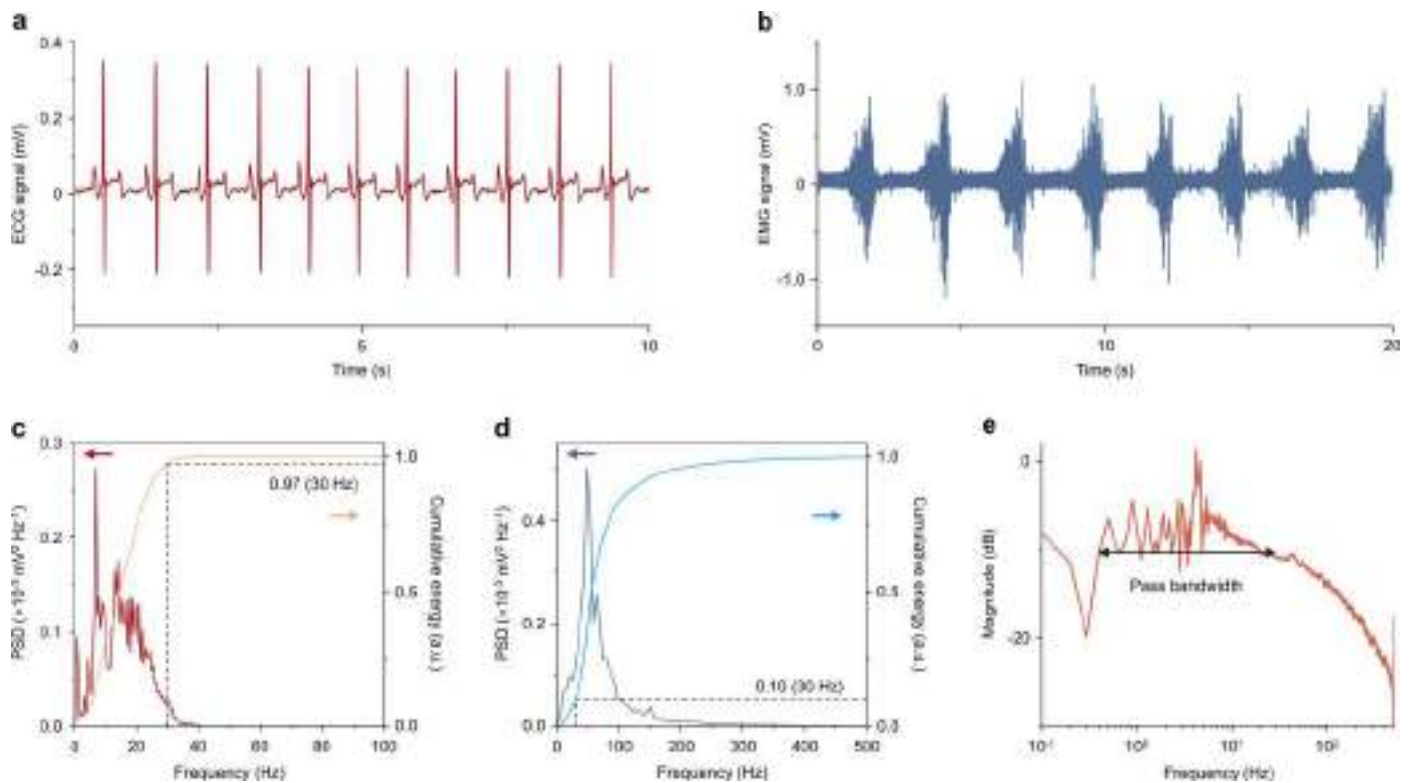
Extended Data Fig. 3 | Thickness-dependent difference of precipitation structures and damping performance. **a-c**, Optical images of the precipitation patterns formed in hydrogels with different thicknesses, **(a)** 2 mm, **(b)** 4 mm, **(c)** 1 mm. The images on the right side of figure **(b)** show the cross-sectional morphology of the 4 mm hydrogel, where the precipitation bands do not fully penetrate through (Scale bars in surface morphologies, 5 mm; Scale bars in cross section, 2 mm). The precipitation patterns show dependence on thickness, there was well-defined periodic bands in the 2 mm hydrogel. And for the thicker hydrogel (4 mm), the bands appear only in the upper region because the downward diffusion of Cu^{2+} has a limited effective depth, and only the near-surface zone reaches the supersaturated concentration. In

contrast, the 1 mm hydrogel generates discrete precipitation spots rather than continuous rings. This occurs because the very thin geometry amplifies local ion-concentration fluctuations, destabilizing the reaction front and causing it to fragment into isolated nucleation domains. Experiments were independently repeated at least three times with similar results. **d-f**, Evaluation of mechanical damping performance for metahydrogels with different matrix thickness and precipitation structures. For the 4 mm sample, the amplitude of the applied mechanical noise was modulated to assess the stability of its damping performance. **g-i**, Magnitude spectra calculated from the amplitude response of each sample relative to the reference signal.



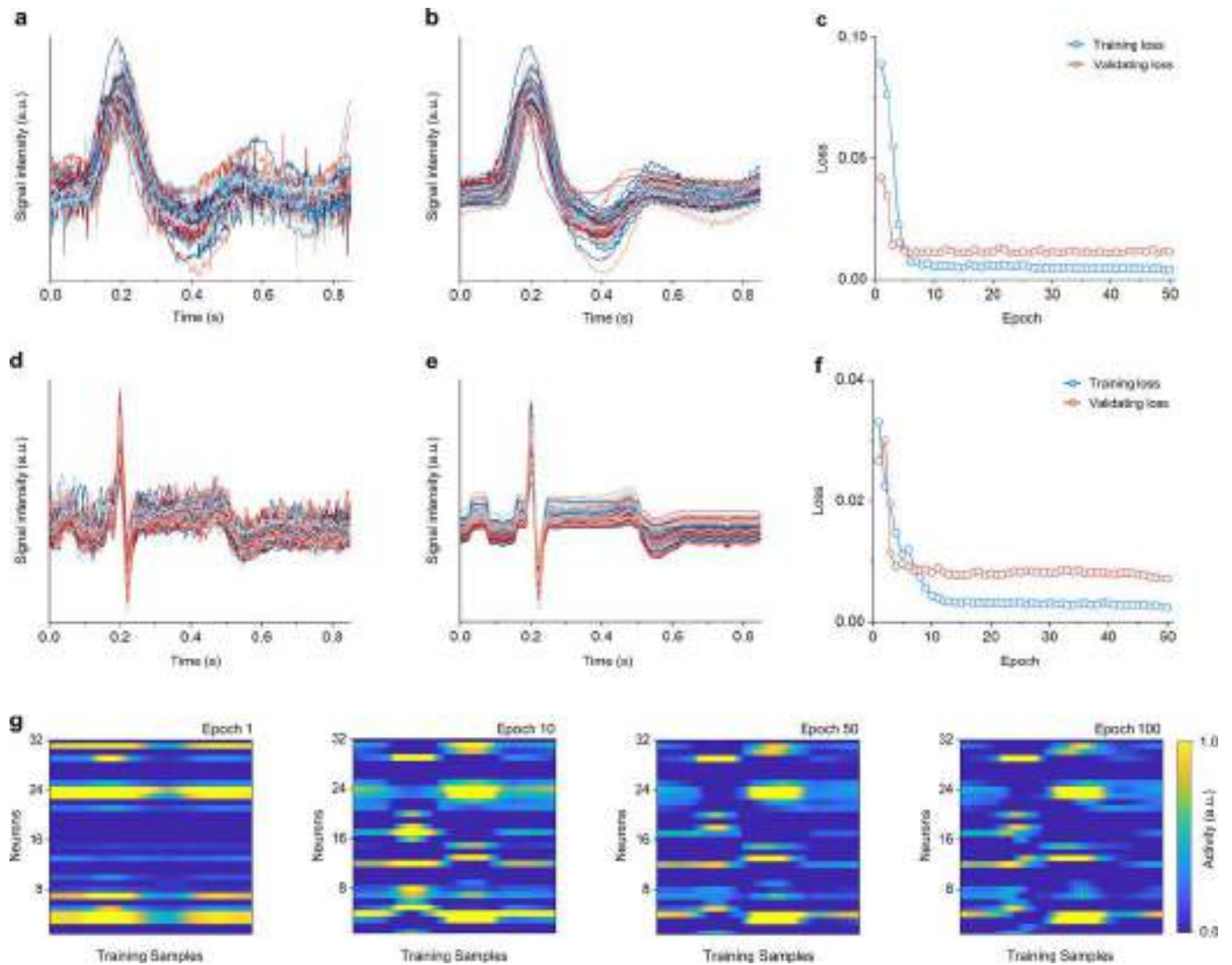
Extended Data Fig. 4 | Metastructural precipitation in different material systems. **a**, Metahydrogel library involving four categories of compound precipitation, including metalates, nonmetalates, hydroxides and halides. Based on the unique diffusion coefficient and precipitation reaction constant of each material, the resulting precipitation patterns exhibit three distinct modes: discrete rings (Blue dot), diffused rings (Orange dot), and hybrid structures (Blue and orange dots) of **b**, Calculated filtered frequency ranges (Shadow regions) of

metahydrogels within different material systems based on their morphologies. The lower line indicates the selected structural factor of different simulative system (Square points), while the upper line represents modulus value defined in the simulation (Circular points). **c**, Statistical distribution of damping frequency ranges of the soft metastructural system with different mechanical properties and structural factors, the mapping diagram represents the overall damping frequency ranges.



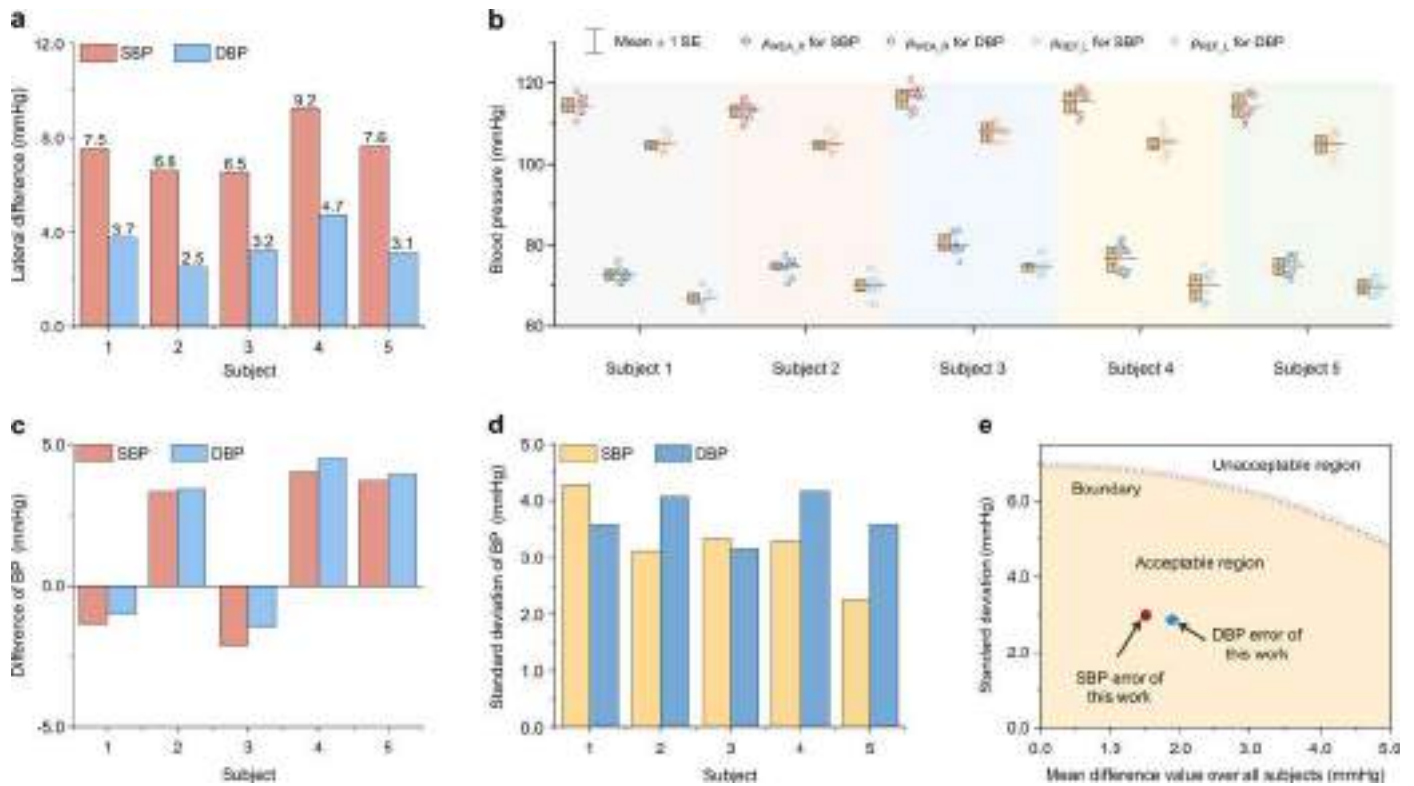
Extended Data Fig. 5 | Frequency-dependent power and energy profiles of ECG and EMG signals. **a-b**, Collected representative ECG and EMG signals for analysis of power and energy profiles. **c-d**, Power spectral density (PSD) and cumulative energy distributions derived from the ECG and EMG signals, with the energy

contributions below 30 Hz highlighted for comparison. **e**, Transfer-function magnitude spectrum of the metahydrogel showing its electrical damping performance. Using -10 dB as the threshold, the characteristic passband is approximately 0.3-30 Hz.



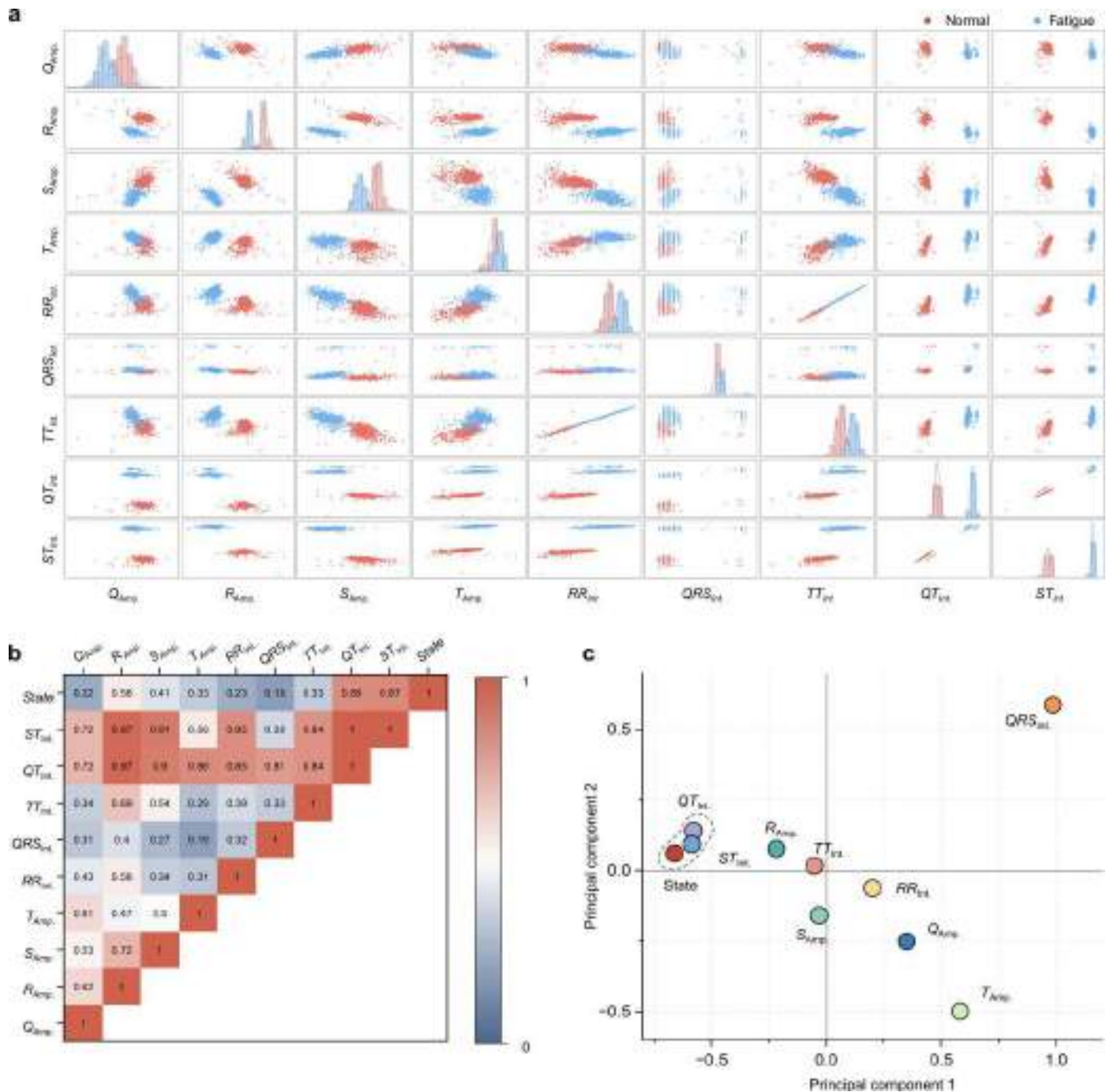
Extended Data Fig. 6 | Physiological signal processing via autoencoder denoising algorithm. a-e, AP (**a, b**) and ECG (**d, e**) signals before and after processing by the autoencoder denoising algorithm. The process effectively removed the unstructured noise in AP and ECG signals. **c-f**, Evaluation of denoising model accuracy as well as loss function during the training epochs.

With training of fewer than 10 epochs, the model can reach a stable state, demonstrating its efficiency. **g**, Visualization of neurons activity during the training process of autoencoder model. After more than 10 training epochs, the neuron states remained stable, confirming that the model had reached a steady state.



Extended Data Fig. 7 | BP monitoring accuracy assessment following the ISO-81060-2 standard. **a**, Lateral difference (*LD*) between the left and right arms of different subjects. Each subject was measured three times, and the average *LD* was used as the final reference. **b**, Statistical comparison of SBP and DBP measured using the MAP-based piezoelectric sensor and the auscultatory method across different subjects, $n = 10$ for each BP data point in the boxplots.

c-d, Mean errors (**c**) and standard deviations (**d**) of the blood pressure measurements obtained for each subject collected by the wearable sensor based on opposite-limb simultaneous method. **e**, Inter-subject errors of SBP and DBP measurements. The red symbol-lines denote the boundary limits of the acceptable region defined by ISO 81060-2, and the yellow-shaded area represents the acceptable region.



Extended Data Fig. 8 | Correlation analysis between ECG features and fatigue states. **a**, Histograms and scatter plots of ECG signal features in normal and fatigue states. The spatial separability of the data points indicates their importance in discriminating different physiological states. **b**, Pearson correlation coefficient between different ECG features parameters and fatigue

state. **c**, Dimensionality reduction and principal component analysis (PCA) results of different ECG features in relation to fatigue state, the clustering distribution suggests QT_{int} and ST_{int} are more effective indicators for identifying physiological state.

Reporting Summary

Nature Portfolio wishes to improve the reproducibility of the work that we publish. This form provides structure for consistency and transparency in reporting. For further information on Nature Portfolio policies, see our [Editorial Policies](#) and the [Editorial Policy Checklist](#).

Statistics

For all statistical analyses, confirm that the following items are present in the figure legend, table legend, main text, or Methods section.

n/a Confirmed

- The exact sample size (n) for each experimental group/condition, given as a discrete number and unit of measurement
- A statement on whether measurements were taken from distinct samples or whether the same sample was measured repeatedly
- The statistical test(s) used AND whether they are one- or two-sided
Only common tests should be described solely by name; describe more complex techniques in the Methods section.
- A description of all covariates tested
- A description of any assumptions or corrections, such as tests of normality and adjustment for multiple comparisons
- A full description of the statistical parameters including central tendency (e.g. means) or other basic estimates (e.g. regression coefficient) AND variation (e.g. standard deviation) or associated estimates of uncertainty (e.g. confidence intervals)
- For null hypothesis testing, the test statistic (e.g. F , t , r) with confidence intervals, effect sizes, degrees of freedom and P value noted
Give P values as exact values whenever suitable.
- For Bayesian analysis, information on the choice of priors and Markov chain Monte Carlo settings
- For hierarchical and complex designs, identification of the appropriate level for tests and full reporting of outcomes
- Estimates of effect sizes (e.g. Cohen's d , Pearson's r), indicating how they were calculated

Our web collection on [statistics for biologists](#) contains articles on many of the points above.

Software and code

Policy information about [availability of computer code](#)

Data collection	The electromechanical and electrochemical properties of metahydrogel were measured by source meters (Keithley 6517B, Keithley 2602 and SR560) and electrochemical workstation (CHI660E). The mechanical and dielectric damping properties were collected by rheometer (MCR 302) and broadband dielectric spectroscopy (Concept 80). Biopac MP46 and self-develop hardware were used for on-body data collection.
Data analysis	Data analysis was performed by commercial softwares. Excel, Origin 2024 and MATLAB R2022a were used to analyze most of the data, plot the data and calculate the statistical parameters. De-noising algorithm and machine learning were done using Python. The code used to visualize the ion kinetic diffusion, extract and analyze the physiological features are available in the repository at https://github.com/TianGuoN/Metahydrogel .

For manuscripts utilizing custom algorithms or software that are central to the research but not yet described in published literature, software must be made available to editors and reviewers. We strongly encourage code deposition in a community repository (e.g. GitHub). See the Nature Portfolio [guidelines for submitting code & software](#) for further information.

Data

Policy information about [availability of data](#)

All manuscripts must include a [data availability statement](#). This statement should provide the following information, where applicable:

- Accession codes, unique identifiers, or web links for publicly available datasets
- A description of any restrictions on data availability
- For clinical datasets or third party data, please ensure that the statement adheres to our [policy](#)

The data supporting the findings of this study are available within the paper and its Supplementary Information files. Source data are provided with this paper.

Research involving human participants, their data, or biological material

Policy information about studies with [human participants or human data](#). See also policy information about [sex, gender \(identity/presentation\), and sexual orientation](#) and [race, ethnicity and racism](#).

Reporting on sex and gender	Sex and gender were not considered as variables in this study. The work primarily investigates fatigue monitoring based on physiological signal characteristics rather than social or biological factors. In the context of fatigue research, variations are more strongly influenced by individual physiological conditions, workload, and environmental factors.
Reporting on race, ethnicity, or other socially relevant groupings	This study did not involve the collection or analysis of data related to race, ethnicity, or other socially defined groups.
Population characteristics	The study cohort consisted of healthy adult participants aged between 20 and 45 years, with a body mass index (BMI) of 18–25 kg m ⁻² . All participants had no history of major diseases within one year prior to the study. Only physiological data collected under different fatigue states were analyzed, and no additional demographic or medical information was considered.
Recruitment	All the participating subjects recruited from Southwest Jiaotong University campus, the neighboring communities through advertisement by posted notices, word of mouth, and email distribution. There were no self-selection biases or other biases. All participants gave consent before participation in the study.
Ethics oversight	All testing from human participants is approved by the Institutional Review Boards (IRB) of Southwest Jiaotong University with the reference number of SWJTU-23012-NSFC(133).

Note that full information on the approval of the study protocol must also be provided in the manuscript.

Field-specific reporting

Please select the one below that is the best fit for your research. If you are not sure, read the appropriate sections before making your selection.

Life sciences Behavioural & social sciences Ecological, evolutionary & environmental sciences

For a reference copy of the document with all sections, see [nature.com/documents/nr-reporting-summary-flat.pdf](https://www.nature.com/documents/nr-reporting-summary-flat.pdf)

Life sciences study design

All studies must disclose on these points even when the disclosure is negative.

Sample size	For on body validation tests, 5 healthy subjects were recruited, and 1 participant was recruited for long-term continuous monitoring of physiological and fatigue states. The sample size was determined based on standards in the literature for proof-of-concept experiments.
Data exclusions	No data exclusion.
Replication	Results were replicated in independent experiments as described in the manuscript. Every measurement included replicates as described in the figure legends and experimental methods.
Randomization	Randomization was not applicable to this study, as no experimental or control groups were established. All participants underwent the same sensing and data acquisition procedures under controlled conditions.
Blinding	Not relevant, because the blinding process would not influence the sampling result.

Reporting for specific materials, systems and methods

We require information from authors about some types of materials, experimental systems and methods used in many studies. Here, indicate whether each material, system or method listed is relevant to your study. If you are not sure if a list item applies to your research, read the appropriate section before selecting a response.

Materials & experimental systems

- n/a Involved in the study
- Antibodies
- Eukaryotic cell lines
- Palaeontology and archaeology
- Animals and other organisms
- Clinical data
- Dual use research of concern
- Plants

Methods

- n/a Involved in the study
- ChIP-seq
- Flow cytometry
- MRI-based neuroimaging

Eukaryotic cell lines

Policy information about [cell lines and Sex and Gender in Research](#)

- Cell line source(s)
- Authentication
- Mycoplasma contamination
- Commonly misidentified lines
(See [ICLAC](#) register)

Plants

- Seed stocks
- Novel plant genotypes
- Authentication